

AD-A178 876

INVESTIGATIONS OF THE POLAR RAIN: POLAR CAP ELECTRON
PRECIPITATION(U) AIR FORCE INST OF TECH
WRIGHT-PATTERSON AFB OH SCHOOL OF ENGINEERING

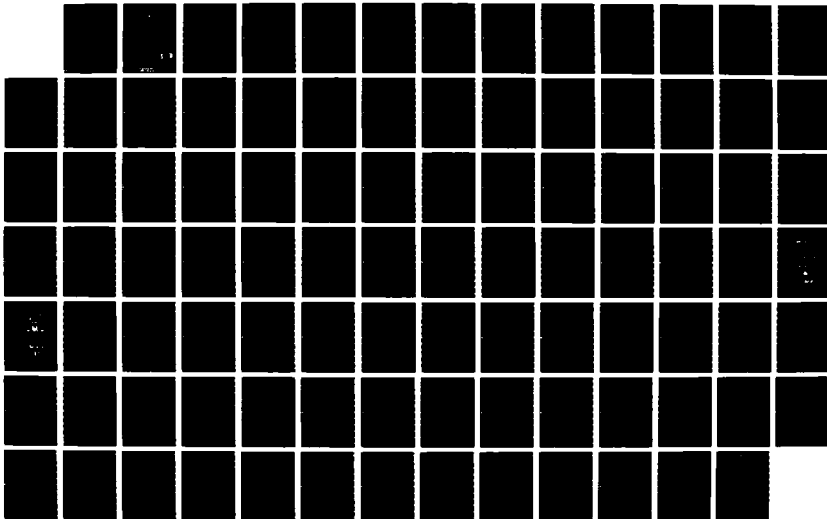
1/1

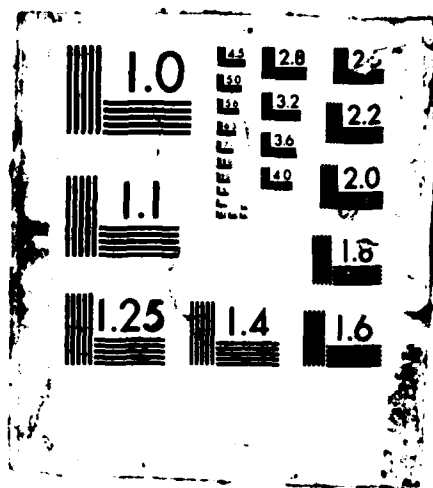
UNCLASSIFIED

K B RIEHL DEC 86 AFIT/GEP/ENP/86D-8

F/G 4/1

NL





①

AD-A178 876



INVESTIGATIONS OF THE POLAR RAIN:
POLAR CAP ELECTRON PRECIPITATION

THESIS

Kevin B. Riehl
Captain, USAF

AFIT/GEP/ENP/86D-8

DTIC
ELECTE
APR 13 1987

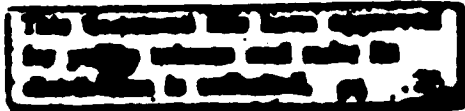
S D
E

DEPARTMENT OF THE AIR FORCE
AIR UNIVERSITY

AIR FORCE INSTITUTE OF TECHNOLOGY

Wright-Patterson Air Force Base, Ohio

87 4 10 087



AFIT/GEP/ENP/86

INVESTIGATIONS OF THE POLAR RAIN:
POLAR CAP ELECTRON PRECIPITATION

THESIS

Kevin B. Riehl
Captain, USAF

AFIT/GEP/ENP/86D-8

DTIC
ELECTE
APR 13 1987
S D
E

Approved for public release; distribution unlimited

INVESTIGATION OF THE POLAR RAIN:
POLAR CAP ELECTRON PRECIPITATION

THESIS

Presented to the Faculty of the School of Engineering
of the Air Force Institute of Technology
Air University
In Partial Fulfillment of the
Requirements for the Degree of
Master of Science in Engineering Physics



Kevin B. Riehl, B.S.
Captain, USAF

December 1986

Accession For	
NTIS GRA&I	<input checked="" type="checkbox"/>
DTIC TAB	<input type="checkbox"/>
Unannounced	<input type="checkbox"/>
Justification	
By _____	
Distribution/	
Availability Codes	
Dist	Avail and/or Special
A-1	

PREFACE

When I originally planned to enter AFIT, I did so hoping to expand both my physics knowledge and confidence. This study has helped me to achieve those goals. Although I had done related work previously, it was done mechanically and without understanding. This thesis forced me to delve deep into the literature and gain a much broader knowledge of solar-magnetospheric physics than I previously had. Even though this study did not go as far as originally intended, I still benefited immensely from this effort.

I must immediately thank my thesis advisor, Major James Lupo, for taking on this thesis. Major Lupo maintained a perfect profile, stepping in when necessary but not directing the research effort. I will miss our useful discussions on the latest literature.

I must also thank Dr David Hardy, my sponsor at the Air Force Geophysics Lab, for his fresh ideas and his support in resolving graphics and computer problems. For his help in running his magnetic field models for me, and the useful conversation he provided, I express my gratitude to my friend Captain (soon to be Dr) Perry Malcolm. Most importantly, I thank Dianne and Brian, my wife and son, for their never ending support.

Kevin B. Riehl

TABLE OF CONTENTS

	Page
Preface	ii
List of Figures	iv
List of Tables	v
Abstract	vi
I. Introduction	1
II. Space Physics Overview	3
Magnetosphere	3
Solar Wind	4
Interplanetary Magnetic Field	6
Particle Precipitation	7
III. Recent Theoretical and Experimental Work	9
IMF Impact on the Polar Rain	9
Polar Rain Plasma Characteristics	16
The Solar Wind and the Magnetosheath/Mantle/Cusp	18
Plasma Characteristics	18
Source of the Polar Rain	20
IV. Instrument and Satellite Characteristics	26
V. Data Analysis	31
Selection	31
Processing	33
Noise Sources	35
VI. Results and Discussion	44
VII. Suggestions and Recommendations	63
Appendix A: Conversion of SSJ/4 Counts to Useful Quantities	65
Appendix B: Noise Correction	71
Bibliography	78
Vita	84

LIST OF FIGURES

Figure	Page
1. The Magnetosphere	4
2. Solar-Magnetospheric Coordinate System	6
3. Reconnection in the Presence of B_x	14
4. Reconnection for Toward and Away IMF Sectors	23
5. Sample DMSF-F6 Trajectories	
a. January, 1983	28
b. May/June, 1983	29
6. Polar Rain Event	32
7. Noise Correction of Distribution Function Values Characterized by a Double Maxwellian	40
8. IMF Control of Dawn/Dusk Gradients	
a. Winter, 1983	46
b. Late Spring, 1983	47
9. Polar Rain Temperatures	50
10. Solar Wind Velocity Versus Polar Rain Temperature	
a. All Cases	52
b. Preferred Cap	53
11. Integral Flux Versus IMF Components	
a. B_x	55
b. B_y	56
12. Solar Wind Density Versus Polar Rain Density	
a. All Cases	57
b. Preferred Cap	58
A. Vector Relationships Between Velocity and Unit Area	65
B. Noise Analysis	
1. Channel 11	74
2. Channel 12	75

LIST OF TABLES

Table	Page
1. Relative Importance of Solar Wind and Radiation Losses to the Sun	5
2. Summary of Electron Plasma Characteristics in the Deep Tail	8
3. Sample Polar Rain Interval from March 16, 1983	38
4. Fitting Process for a Single Maxwellian	41
5. Pitch Angle Mapping of the Deep Tail Electron Distribution to Lower Altitudes	61
A. Count Rate Generated by a Perfect Double Maxwellian Distribution	69
B. Summary of Systematic Corrections for Noise in Channels 11 and 12	77

ABSTRACT

A study of the characteristics of the polar rain using data from the SSJ/4 sensor on the Defense Meteorological Satellite Program F6 satellite has been performed. Recent literature on the polar rain is reviewed. Dawn/dusk flux gradients are verified as being controlled by the interplanetary magnetic field (IMF) Y-component at least 84% of the time. The IMF Z-component is shown to play a role in generating flux gradients. The polar rain is best characterized by a double Maxwellian distribution with typical temperatures of 80-90 eV for the low energy component and 3.6-4.8 keV for the high energy component. The characteristics of the low energy component of the polar rain strongly match those of the solar wind strahl component, suggesting the polar rain is of strahl origin. But correlations with IMF sector structure and solar wind parameters do not show the relationships proposed by Fairfield and Scudder (1985), since the "unpreferred" cap generally has the same polar rain characteristics as the "preferred" cap.

INVESTIGATIONS OF THE POLAR RAIN:
POLAR CAP ELECTRON PRECIPITATION

I. INTRODUCTION

It is well known that charged particles are constantly bombarding the region above the earth's polar caps (O'Brien, 1964, and articles within). This particle flux may increase orders of magnitude during magnetic storms (Akasofu, 1968: 212-217), disabling communication and radar systems which depend on normal environmental conditions in the polar regions (Fremouw and Wittwer, 1984:98). For example, a recent major magnetic storm caused high frequency radio link outages, serious power surges on long lines, and even a Canadian legal battle questioning whether storm induced potentials could have affected a microwave traffic control device that caused a head-on train collision (Allen, 1986).

Since the northern pole is critical to U.S. military detection and communication systems, the Air Force has an interest in knowing when such events will occur. Monitoring changes in the interplanetary magnetic field detected sunward of the earth may be able to predict changes in particle flux at the poles. Studies, such as this thesis, are being performed to better understand the solar-terrestrial relationships which control the particle flux.

Large spatial and temporal variations of the flux in-

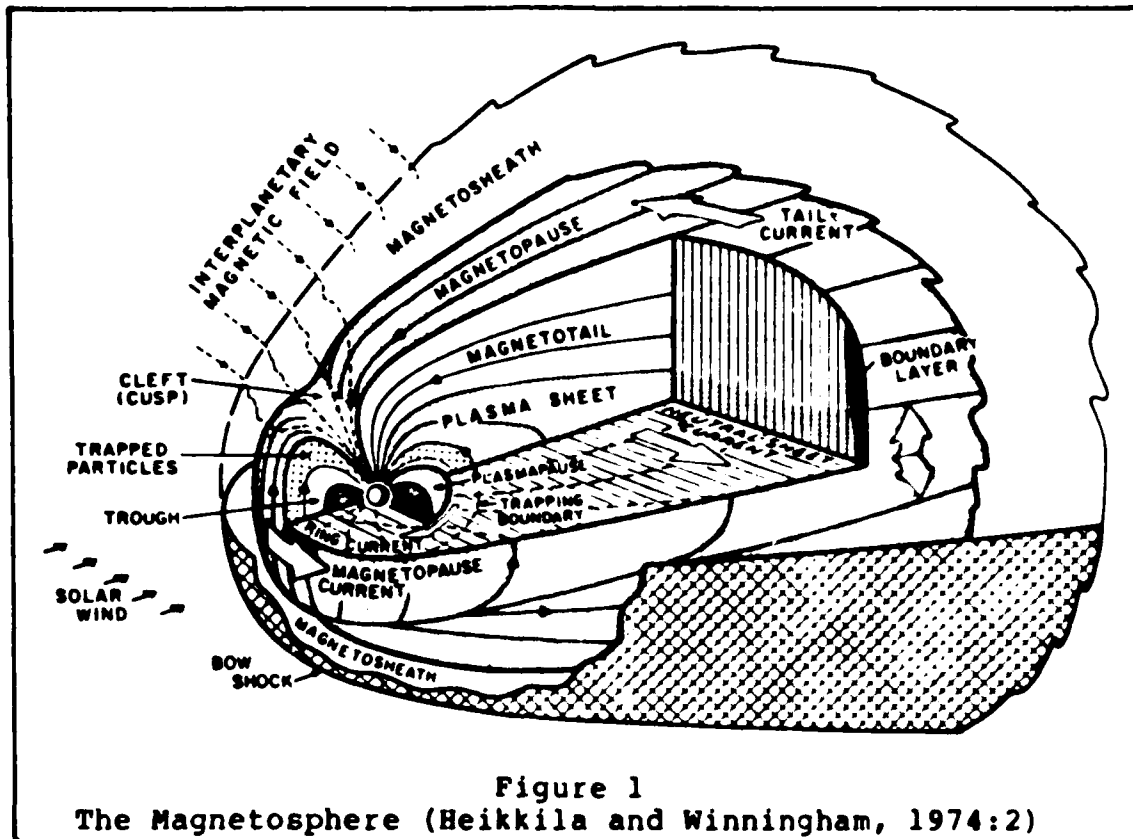
tensities make it difficult to identify the processes generating precipitating particles. The particles are both positively and negatively charged, with electrons being the dominant species. This thesis will examine electron precipitation, termed the "polar rain", at latitudes poleward of the well known auroral regions. Although a small contributor to the dynamic events noted above, the polar rain is a fairly stable phenomena, with simpler and more direct connections to the interplanetary field. This makes it an excellent indicator of magnetospheric topology and its responses to the solar wind and interplanetary magnetic field (Yeager and Frank, 1976:3966). It will be shown that the polar rain responds to the interplanetary magnetic field in a predictable manner and that the source of the polar rain is the strahl component of the solar wind.

II. SPACE PHYSICS OVERVIEW

Magnetosphere

The earth's magnetic field is a perturbed dipole, the result of the solar wind confining the geomagnetic field to a cavity known as the magnetosphere (fig 1). The figure shows the complex nature of the magnetosphere. The solar wind compresses the earth's magnetic field on the side facing the sun and stretches the field lines into a long tail, called the "magnetotail", away from the sun. The magnetosphere extends ~10 earth radii towards the sun. In front of the magnetosphere is the "bow shock", the shock formed by the supersonic flow of the solar wind. The "magnetopause" is the magnetospheric surface which the solar wind hits after passing through the bow shock. The "magnetosheath" is the region between the bow shock and the magnetopause, and is characterized as a region of plasma turbulence. The plasmopause is the surface formed by the "last" closed geomagnetic field line (summary from Schulz and Lanzerotti, 1974:1-6).

It is common to think of the magnetosphere as containing "open" and "closed" magnetic field lines. Closed field lines create magnetic mirrors, which confine charged particles into the radiation belts and create the auroral region through the loss cone. The open field lines are at higher latitudes than the auroral boundary and are so termed



because they travel far back into the magnetotail and never actually close due to reconnection with the interplanetary magnetic field. Although charged particles may also mirror on open field lines, a reflection would cause the particle to be "lost" as it travels away from the polar cap into the deep tail or interplanetary space (Baker and others, 1986).

Solar Wind

Between the magnetosphere and the sun is interplanetary space dominated by the solar wind plasma and the interplanetary magnetic field (IMF). The solar wind is a neutral ionized gas containing ions and electrons. It is a consequence of the continual expansion of the hot solar corona

TABLE I
Relative Importance of Solar Wind and Radiation
Losses to the Sun (Axford, 1985: 575)

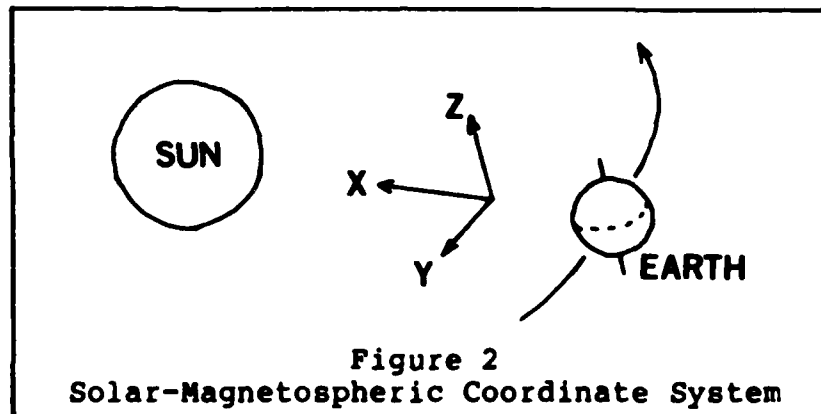
	<u>Solar Wind</u>	<u>Radiation</u>
Mass loss rate	10^{12} g/s	4×10^{12} g/s
Energy flux (1 AU)	$.16$ erg/cm ² -s	1.4×10^6 erg/cm ² -s
Momentum flux (1 AU)	8×10^{-9} g/cm-s	5×10^{-5} g/cm-s
Despin time	10^{10} yr	10^{12} yr

(Parker, 1962:461). Although the solar wind plays a key role in the earth's upper atmosphere and polar caps, Table I shows the solar wind is only important to the sun as an angular momentum loss. Black-body radiation dominates the mass loss, energy flux, and momentum flux. The thermal and magnetic energy densities are small, so that over 99% of the solar wind energy density is kinetic at 1 astronomical unit (AU) (Pneuman, 1986:107).

Recent solar wind models are summarized by Axford (1985) and Cuperman (1983). Experimental data, (see, for example, Feldman and others, 1975; Rosenbauer and others, 1977; Scudder and Olbert, 1979; Pilipp and others, 1985) indicates the solar wind usually has a double nearly maxwellian distribution with an anisotropic high energy tail. The solar wind has typical velocities of 400-600 km/s and electron densities of 5-25 e⁻/cm³. The velocity and density are curiously coupled such that their product is fairly stable, even over solar cycle (Pneuman, 1986:107).

Interplanetary Magnetic Field

The interplanetary magnetic field is the magnetic field which lies in interplanetary space and is the sum of all magnetic field contributors in the solar system. Dominated by the sun's magnetic field, the IMF vector oscillates both in direction and magnitude. Usually represented by the solar-magnetosphere coordinate system (see fig 2), each of the three components will range from positive to negative within a period of days. The effect of the IMF on the magnetospheric topology and particle precipitation is dramatic. Magnetic reconnection is discussed by Axford (1984)



and Cowley (1973). Theoretical modelling of IMF perturbations to the magnetosphere is presented, for example, by Cowley (1981a,b), Akasofu and others (1981), and Nishida (1983). Experimental data exhibiting IMF influence on particle precipitation is seen in works by Yeager and Frank (1976), Baker and others (1981), Gussenhoven and others (1984), and Riehl and Hardy (1986).

IMF and solar wind data are gathered by a satellite

(presently IMP-8) when it is positioned in front of the bow shock. IMF components have typical magnitudes of a few gamma (1 gamma=1 nanotesla). Solar wind and IMF data for the last few years has been compiled into hourly averages by Couzens and King (1986). This reference will be the source of solar wind and IMF data presented in this thesis.

Particle Precipitation

Since the discovery of the earth's radiation belts (Van Allen and others, 1958), it has been known that the magnetosphere contains a wealth of charged particles. These particles have an orientation with respect to the magnetic field such that they travel along magnetic field lines to an altitude where they either mirror or are lost into the earth's atmosphere. Electric fields may also be present, accelerating the particles. Analysis of such precipitating particles has been on-going for over 20 years (see, for example, O'Brien, 1964, and Akasofu, 1968:174-211).

There are distinct local source regions for electron precipitations. The most energetic source is the radiation belts, which feed precipitating particles into the auroral zone. Auroral zone flux levels (see, for example, Hardy, 1985) average around 10^9 e⁻/cm²-s-sr and dump roughly 10^{10} watts into the ionosphere (Burke and others, 1982:2). Other sources of precipitating particles include the magnetosheath (Eastman and others, 1976), the cusp, the plasma sheet (Cattell and others, 1986), and the magnetotail lobes. Each

TABLE II

Summary of Electron Plasma Characteristics in
the Deep Tail (Bame and others, 1983:913)

<u>Location</u>	<u>Density</u>	<u>Drift Speed</u>	<u>Temperature</u>
Magnetosheath	8 cm ⁻³	500 km/s *	17 eV
Low altitude boundary layer	1	200 *	69
Mantle	1	250 *	26
Plasma Sheet	.6	500 *	78
Lobe	.04	?	69

* flow is anti-sunward

of these regions are distinct because of differences in the local magnetic field strength, plasma temperature and density, and the dominant direction of particle motion. Table II gives a summary of some typical values of electron characteristics in some of these regions, as measured in the deep tail. This thesis will examine electrons thought to have travelled through the magnetotail lobes (Fairfield and Scudder, 1985, and Baker and others, 1986).

III. RECENT THEORETICAL AND EXPERIMENTAL WORK

The polar rain was first identified by Winningham and Heikkila (1974). It is best characterized as a weak, uniform electron precipitation present across the entire cap above the auroral boundary (above the last closed geomagnetic field line). It is known to have average energies of about 100 eV and to be approximately isotropic. There has been a recent burst of polar rain research including works by Gussenhoven and others (1984), Fairfield and Scudder (1985), Riehl and Hardy (1986), and Baker and others (1986). It is the intent of this Section to review the recent theoretical and experimental phenomena associated with the polar rain.

IMF Impact on the Polar Rain

The entrance mechanism of precipitating particles to low altitudes is only generally understood. There is widespread agreement that the ultimate source is the solar wind, but the space physics community does not agree on the precise solar wind-magnetosphere interaction process by which the particles arrive at the polar caps. It was originally thought that the magnetosphere was closed--no IMF lines penetrated or connected to the earth's magnetic field lines. This would imply that particles enter the magnetosphere by diffusing across magnetic field lines and, therefore, that all low altitude electrons would be considered of magneto-

spheric origin. The IMF polarity would have little effect on these electrons.

It was Dungey (1961) who first advocated an open magnetosphere and theorized that IMF fluctuations would play a role in perturbing the earth's magnetic field. Today, "there exists a large body of evidence suggesting" (Stern, 1984:200) the magnetosphere is open (fig 1 shows a partially open magnetosphere). The open magnetosphere allows for reconnection of some magnetospheric field lines with the IMF. Under such an arrangement, each of the IMF components (B_x , B_y , B_z) will have a dramatic effect on the characteristics of the polar rain.

The cause of variations in the IMF are not well understood. Part of the cause of the B_x and B_y fluctuations is that the sun's dipole axis is offset 20° from its rotation axis (Akasofu and Fry, 1985:18). This will contribute an oscillatory baseline to B_x and B_y . There are obviously other unidentified contributors to these equatorial IMF components, since B_x and B_y oscillate over a much shorter period (roughly 7-10 days) than the period of the sun's rotation (27 days).

It is somewhat easier to envision variations in B_x and B_y than in B_z , since a southward pointing IMF implies the sun's dipole field has been turned upside down! Suggested causes of B_z reversals include (summarized in Akasofu and Fry, 1985:13-18, and Akasofu and Lee, 1986:3-5) solar

flares, "magnetic clouds", equatorial "transients", and the so-called "magnetic tongue". The causes of B_z variations are very poorly understood, partly because it has fallen in the gap between solar physics and magnetospheric physics (Akasofu, 1983:181). For the purpose of this thesis, let it suffice to say all IMF components suffer reversals, with B_z being more unpredictable than B_x and B_y .

B_z plays a crucial role in determining the amount of solar wind energy transferred to the magnetosphere (for example, Akasofu and Lee, 1986; Akasofu and others, 1981; and Nishida, 1983). The solar wind has the best access to the magnetosphere when B_z is southward, due to reconnection between the IMF and the dayside magnetosphere. Akasofu and others (1981) applied a simple superposition model to the IMF and magnetosphere (what Cowley, 1981a, refers to as "dipole plus uniform IMF") to show the northern cap becomes very open (large region of open field lines) when B_z is neutral to southward. They also showed that B_y plays a small role in opening the cap and that the cap was virtually closed when B_z is strongly positive. Unfortunately, Akasofu and others showed no southern cap results.

The conclusion of this type of modeling is that a southward IMF is a requirement for a large region of open field lines. One would anticipate this is also a requirement for extended polar rain, if the polar rain originates on open field lines. Indeed, Gussenhoven and others (1984)

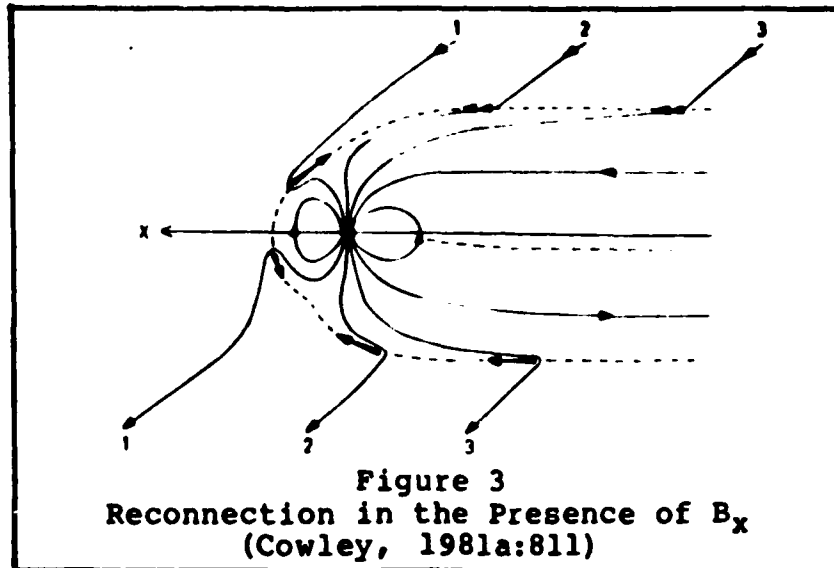
and Riehl and Hardy (1986) showed the dominant condition for the polar rain was for B_z to be neutral to southward, which is interpreted as support that the polar rain originates on open magnetic field lines.

It should be noted that there is not total agreement that the polar rain originates on open field lines. Heikkila (1984) notes that quite often a trapped pitch angle distribution of a weak particle flux is seen poleward of the auroral oval. He uses this evidence (which he doesn't reference), along with the fact that there is a large (5° - 15°) poleward movement of recovery phase auroral forms, to argue that the region of open field lines is smaller than previously thought. He concedes some open field lines re-connect with the IMF, but that there is a boundary layer of magnetosheath plasma inside the magnetopause, at least partly on closed field lines, which can precipitate to the polar regions.

Further clouding the issue is the work of Hardy (1984b). Winningham and Heikkila (1974) identified three types of electron precipitation in their study. In addition to the polar rain, they identified more intense and energetic precipitations which they termed polar "squalls" and polar "showers". The squalls and showers are now known to be associated with magnetically disturbed intervals; Hardy (1984b) showed the dominant condition for both (the polar showers were identified as polar cap auroral arcs) was for

B_z to be northward. $B_z > 0$ implies the squalls and showers are on closed field lines, but Hardy noted they are detached from the auroral oval. The observation that polar cap arcs and polar rain can occur alternately across the cap led him to propose the intense precipitations were also on open field lines. Based upon the conflicting ideas of Heikkila and Hardy, it should be clear that the issue of open/closed magnetic field lines and their relationship to polar cap precipitation is hardly resolved.

The IMF B_x component is thought (for example, Cowley, 1981a) to control preferential electron flux into one polar cap or the other. This is a result of dayside magnetic flux tubes moving poleward and opening (in both poles), but the magnetopause-IMF intersection point moving sunward, creating a bundle of open field lines in the connected pole. Figure 3 shows the reconnection of the IMF with the magnetosphere when $B_x > 0$ and $B_z < 0$. The numbers (1-3) indicate the time sequence as a single IMF line sweeps by the magnetosphere and the dark arrows indicate the flux tube tension (Cowley, 1981a:810-812). The figure indicates preferential reconnection in the southern hemisphere. In the open magnetospheric model (see fig 4), $B_x < 0$ should result in enhanced northern cap particle flux intensities, while $B_x > 0$ should increase the intensity in the south pole (Gosling and others, 1986), since each of these cases result in a larger open cap in the preferred hemisphere.



The first experimental evidence that electron flux intensities varied with B_x was presented by Yeager and Frank (1976). They showed that 305-510 eV electron intensities in the northern near tail (5-10 R_e) corresponded consistently with prediction. Riehl and Hardy (1986) showed flux intensities increased with B_x (and B_y) in the preferred cap, but remained at consistently low levels independent of B_x (and B_y) in the unpreferred cap. Unfortunately, at 1 AU the IMF usually has the "garden hose" angle, which couples B_x and B_y . A "toward" IMF sector is defined as having $B_x > 0$, and almost always B_y is negative. An "away" sector has $B_x < 0$, and almost always B_y is positive. As a result, Yeager and Frank and Riehl and Hardy could only show the electron precipitation corresponds to toward and away sectors; it has been difficult for anyone to decouple B_x and B_y and show that only B_x is responsible for preferential entry of the polar rain to one cap or the other.

In theory, the B_y component controls only particle flux gradients across the cap (Cowley, 1981a,b, and Nishida, 1983). East/west asymmetries are exerted on open magnetic flux tubes in the presence of an IMF B_y , resulting in a B_y -dependent torque being exerted about the earth-sun line. The magnetospheric field lines reconnecting with the IMF are dragged azimuthally as the interplanetary end of the field line is stretched away by the solar wind (Nishida, 1983:196-197). This results in a bunching of field lines in one quadrant of the northern lobe and the opposite quadrant of the southern lobe, implying asymmetric addition of open magnetic flux tubes to the magnetotail lobes. When $B_y > 0$, charged particles will preferentially enter the north (south) pole from the dawn (dusk) side. When $B_y < 0$, the opposite should be true.

Meng and others (1977) were the first to report experimental evidence which agreed with the predicted dawn/dusk gradients. Riehl and Hardy (1986) found agreement with Meng and others (and theory) in the northern cap, but noted gradients in the southern cap were unresponsive to the polarity of B_y , tending to always decrease (dawn to dusk) or have no gradient at all. Since the Riehl and Hardy data set was over a relatively short period of time (September to January), the possibility of seasonal dependence (Nishida, 1983:198) or the peculiarities of satellite trajectory exist as possible explanations of this southern hemisphere data.

In an even larger divergence from theory, Gussenhoven and others (1984) reported the dominant polar rain flux gradient was from pre-noon to pre-midnight. They performed a large statistical study in which they binned 12 months of polar rain data into a two-dimensional array of geomagnetic latitude and magnetic local time. They found that $B_y > 0$ ($B_y < 0$) in the northern (southern) cap did shift the noon-midnight gradient towards the dawn side, but there was no reciprocal asymmetry for the reversed IMF configuration (Gussenhoven and others, 1984: 9792). There has been no explanation of this finding, although Gussenhoven and others noted the higher dayside intensities suggested the plasma mantle, the region of transition from the magnetosheath to the tail lobes (Gussenhoven and others, 1984:9793-9794), as a source for the polar rain.

Polar Rain Plasma Characteristics

A number of authors have reported on various characteristics of the polar rain. Yeager and Frank (1976) noted densities of 0.0015-0.045 e^-/cm^3 in the near tail. Barfield (1984), using data from the Dynamics Explorer (DE) -1 and -2 satellites, reported a nearly maxwellian distribution with temperatures of ~ 100 eV and densities of 1-5 e^-/cm^3 . This large density is a result of the detectors measuring down to 5 eV, where there is large contamination of the polar rain with photoelectrons. He also noted a trace of a high energy tail in the polar rain; one example had a double maxwellian

distribution with the lower energy maxwellian having a temperature of 65 eV and the higher energy maxwellian having a temperature of 141 eV. Since DE-1 and DE-2 are in different orbits (circular versus elliptical), Barfield noted the important discovery that the polar rain distributions looked essentially the same at 600 km and 15,000 km. This meant there is no accelerating mechanism between these two altitudes. Ober (1984) showed HILAT satellite distribution function plots exhibiting a clear high energy component (near double maxwellian distributions). Temperatures for the low energy component ranged from ~20-110 eV and the high energy component temperatures ranged from ~800-3500 eV. Gussenhoven and others (1984), reported that the average energy of the polar rain increased considerably from noon to midnight in reciprocal to the flux gradient already discussed.

The most comprehensive characteristics study was performed by Riehl and Hardy (1986). Using 45 s averaging intervals, it was shown the polar rain was characterized by a double maxwellian distribution about 1/3 of the time. The low energy maxwellian was surprisingly well characterized, with an average temperature of 80 eV and a statistical error of only 13 eV, regardless of the spatial and temporal variations of the satellite across the polar cap. The average density of the low energy component was $0.055 \text{ e}^-/\text{cm}^3$. The high energy component, when it did exist, had temperatures

ranging from ~400-2400 eV and had an average density of only $0.0006 \text{ e}^-/\text{cm}^3$. It was noted the ratio of the high energy temperature to the low energy temperature had a prominent peak at ~7-8, but the ratio had values up to about 50. Typical polar rain integral flux values were noted to be $6 \times 10^5 - 5 \times 10^6 \text{ e}^-/\text{cm}^2\text{-s-sr}$.

The Solar Wind and the Magnetosheath/Mantle/Cusp

The most commonly proposed polar rain sources are the magnetosheath/plasma mantle/polar cusp source, and the solar wind (Fairfield and Scudder, 1985; Riehl and Hardy, 1986; Baker and others, 1986). To determine whether either of these source regions map into the polar region, it would be wise to review their characteristics.

Plasma Characteristics

The solar wind is a consequence of the expanding solar corona and is accelerated from its origin to at least 1 AU. Experimental data (see, for example, Feldman and others 1978; Feldman and others, 1975; Rosenbauer and others, 1977) indicates (at 1 AU) the solar wind has a nearly bi-maxwellian distribution with an anisotropic high energy tail. The low energy maxwellian is called the "core". The core carries about 94% of the solar wind density and has a temperature ranging from ~5-12 eV. The higher energy maxwellian is termed the "halo" and has a temperature of ~45-70 eV. The halo to core temperature ratio is usually ~6-10:1.

The anisotropic tail is called the "strahl". The

strahl is highly field aligned (pitch angles of 1° or less) and wasn't discovered until narrow angle detector data was examined (Rosenbauer and others, 1977). The strahl is thought to be due to electrons of the solar corona which have undergone minimal scattering to 1 AU. Strahl electrons are very field aligned because they conserve the first adiabatic invariant (see Schmidt, 1979:5-29, for discussion on adiabatic invariants) as they move away from the sun into a decreasing magnetic field. Lower energy strahl electrons are scattered more than higher energy strahl electrons due to the coulomb collision frequency (which is highly energy dependent) (Fairfield and Scudder, 1985:4058), raising the possibility of two distinct strahl components. Strahl temperatures of 60-175 eV have been reported. Recently, Pilipp and others (1985) have discovered the strahl becomes extremely anisotropic within IMF sectors (toward and away) and cooler and more isotropic at sector boundaries. It has also been noted an enhanced strahl is associated with high speed solar wind streams (Fairfield and Scudder, 1985:4066).

In contrast to the solar wind, the magnetosheath and the plasma mantle are not as well characterized. The magnetosheath is a turbulent region and is the primary source of the mantle. Dayside magnetosheath temperatures are ~ 43 eV (Gosling and others, 1986). This is hotter than the magnetosheath is in the deep tail (Table II) because a stronger interaction with the bow shock occurs on the day-

side (Feldman and others, 1983). Typical magnetosheath densities are $5-10 \text{ e}^-/\text{cm}^3$. The plasma mantle, which has easy access to the cusp region, is somewhat hotter than the magnetosheath in the tail (Table II), but an order of magnitude less dense. No near earth characteristics of the mantle could be found, although the cusp has been noted to have temperatures of $\sim 90-100 \text{ eV}$ and densities of $\sim 0.5 \text{ e}^-/\text{cm}^3$, implying an acceleration mechanism if cusp electrons originate in the mantle.

Source of the Polar Rain

The magnetosheath/mantle/cusp origin of the polar rain was originally proposed because of the similarity of the cusp spectral distribution to the polar rain. Although their temperatures are similar, the intensity of the polar rain is $\sim 1-2$ orders of magnitude less (Heikkila, 1984:??). This led Barfield (1984) to a magnetosheath origin with precipitation via the tail lobes. Gussenhoven and others (1984) advocated the mantle/cusp origin because of the much higher dayside flux intensities they noted in their study. Heikkila (1984) also proposes a magnetosheath source, theorizing pitch angle scattering of electrons at the rotational discontinuity at the lobe magnetopause. Both Heikkila and Gussenhoven and others use the fact that there is a dearth of energetic ions in the polar rain to support their source proposal. The hotter magnetosheath electrons may scatter onto polar field lines, while the tailward traveling ions

are too cold and massive to be scattered enough to become polar rain. Charge neutralization of the polar rain is probably realized with very cold ions generated in the polar wind (the ionosphere).

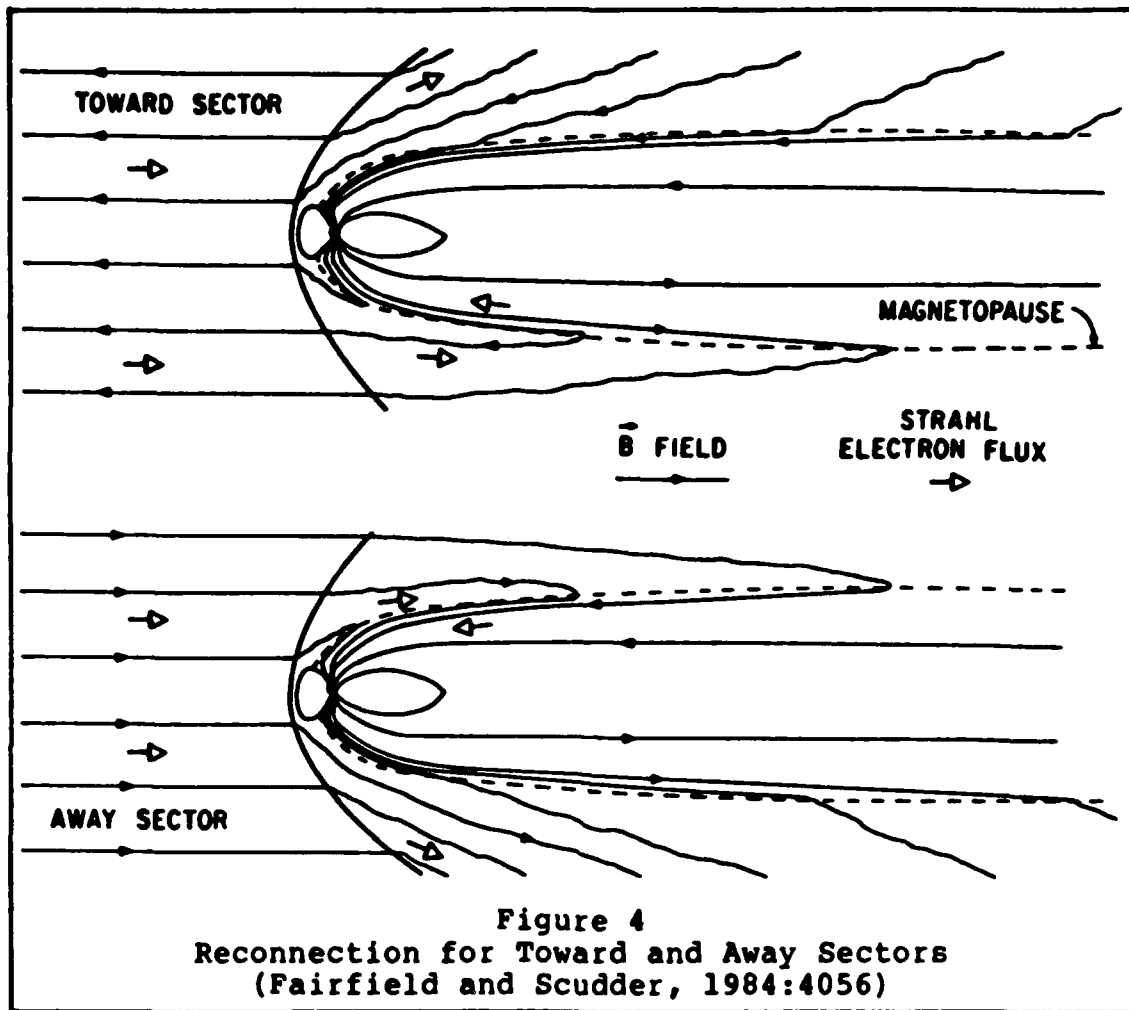
Magnetic reconnection between the IMF and the dayside magnetopause causes transport of open magnetospheric field lines to the magnetotail (Nishida, 1983:189). Stern (1984:205) points out that three-fourths of the frontage of the magnetosphere (from a sun line of sight) involves the tail. So the tail region provides an excellent location for energy input to the magnetosphere.

Two recent polar rain articles have concentrated on the electron distributions in the magnetotail (Fairfield and Scudder, 1985; Baker and others, 1986) and have made a compelling argument that the polar rain is the result of the strahl component of the solar wind. Using data from the International Sun-Earth Explorer (ISEE) -1 satellite, Fairfield and Scudder (1985) discovered that northern tail lobe electrons were extremely field-aligned (anisotropic) and that the electron intensities corresponded with IMF sector structure. They mapped the tail lobe distribution function back into the solar wind and confirmed that the lobe electrons were from the strahl. Since the tail lobe electron distribution functions were similar to the polar rain (Fairfield and Scudder, 1985:4062), they theorized the polar rain is the result of solar coronal electrons, namely,

the strahl.

Since the strahl is a result of the nearly collisionless transit from the inner solar corona to 1 AU, the logical conclusion that a higher solar wind density means a higher polar rain density is incorrect, at least as applied to the strahl source theory. Simply, a higher solar wind density results in more collisions and less strahl electrons making it to the magnetosphere. Thus, Fairfield and Scudder predicted the polar rain density should vary inversely with the solar wind density. This has been verified in only extreme cases (Riehl and Hardy, 1986:1570).

Fairfield and Scudder also proposed asymmetries associated with magnetic sector at high energies (see fig 4). In the preferred cap, the strahl enters the tail lobe and proceeds towards the earth, becoming more and more isotropic with the increasing magnetic field. Under these conditions, Fairfield and Scudder noted some bi-directional streaming (electrons flowing away from the earth as well as towards it). The electrons traveling away from the earth were thought to be tail lobe electrons which had mirrored on open field lines. In the unpreferred cap, only the more isotropic halo distribution should have entry, resulting in an overall lower energy distribution. To account for the elimination of low energy electrons (the solar wind core) in their direct entrance theory, Fairfield and Scudder propose a potential barrier at the magnetopause. It is ironic that



they propose a decelerating mechanism to explain their polar rain source, while Gussenhoven and others (1984) and Heikkila (1984) propose an accelerating mechanism. Yet the direct entry theory relies on the same argument to account for the lack of energetic ions: reflection at the rotational discontinuity at the magnetopause (Stern, 1983).

Baker and others (1986), using data from the ISEE-3 satellite, verified the field-aligned electron distributions seen by Fairfield and Scudder, and made a detailed examination of the bi-directionality. They also verified intensi-

ties in the north and south tail lobes were critically dependent on IMF sector structure according to theory. As ISEE-3 traversed the magnetopause boundary, Baker and others (1986:5654) made the important discovery of direct entry of electrons into the tail lobes. They concluded this was proof of the open magnetospheric model and refuted the closed model proposed by Heikkila (1984).

Baker and others could also follow the electron distributions as they transitioned from uni-directional (toward the earth) to bi-directional. This phenomena was sector dependent as discussed by Fairfield and Scudder, with the unpreferred cap being uni-directional. They also conceded some polar cusp plasma entry (Baker and others, 1986:5660) on the dayside to account for the dominant gradient noted by Gussenhoven and others (1984), but agreed with Fairfield and Scudder that the primary polar rain source is the strahl. They noted bi-directional plasma densities of $0.01-0.1 \text{ cm}^{-3}$.

Riehl and Hardy (1986) noted the low energy maxwellian that was always present in the polar rain agreed quite well with reported strahl temperatures, leading them to also support the strahl source theory. But they were unsuccessful in correlating the solar wind speed and preferred cap structure with the temperature of the polar rain. It was unexplained why the polar rain temperature was so stable in both the preferred and unpreferred caps. The high energy component, which was noted to have a much larger error

associated with the fitting process, also appeared in both caps regardless of sector structure. It is the intent of this thesis to establish a new polar rain data set which provides the opportunity to resolve some of these questions.

IV. INSTRUMENT AND SATELLITE CHARACTERISTICS

Data was used from the SSJ/4 sensor on the F6 satellite of the Defense Meteorological Satellite Program (DMSP). The SSJ/4 sensor consists of two analyzers which each have two cylindrical curved plates. Particles are measured in 20 energy channels in the range from 30 eV to 30 keV, with one analyzer for electrons and the other for ions. This is accomplished by applying a potential across the curved plates, which in turn creates a velocity selector through the resulting electric field. A particle of the appropriate energy will be curved enough to pass through both apertures and strike a channeltron.

The channeltron is an electron multiplier system analogous to a photomultiplier tube. Impact at the front end of the channeltron ejects secondary electrons which collide with the tube walls, creating additional secondaries and thus generating an output pulse (Hardy and others, 1984c:130). Each energy channel is accessed for 98 ms, with 2 ms left to stabilize the plate voltage. With each pair of curved plates, a full 20 channel spectrum is returned once per second.

The SSJ/4 analyzers have rectangular apertures with small opening angles. This introduces small complications in the analysis of the particle distribution functions, as will be discussed later. Due to the finite aperture sizes, each channel accepts a bandwidth of energies which is rough-

ly 10% (full-width half-maximum) of the nominal channel energy.

As with all detectors, calibration is essential to ensure the reliability of the data. Calibration of the SSJ/4 sensor is discussed by Hardy and others (1984a,c), Marshall and others (1986), and an effective summary by Phillips (1984:23-24). The primary goal of the calibration is to determine the energy independent geometric factor, which is the key quantity in converting from raw count rate to physical parameters such as differential flux or distribution function values. The SSJ/4 is a well-calibrated instrument; the geometric factor and energy bandwidth are well known.

The DMSP-F6 satellite was launched in December, 1982. It is maintained in a 840 km circular polar orbit, sun-synchronous in the dawn-dusk meridian plane. The satellite is non-spinning and the SSJ/4 sensor is mounted such that the look angle is always radially out from the earth (Hardy and others, 1984a:4-6). Although DMSP-F6 is in a sun-synchronous orbit, the spatial coverage varies widely due to the diurnal rotation of the earth's magnetic pole about the geomagnetic pole. Sample satellite tracks for winter (January) and late spring (May/June) are shown in fig 5 for each pole. It can be seen the satellite precesses to the dayside in the southern pole and to the nightside in the northern pole, with the precession occurring over a short

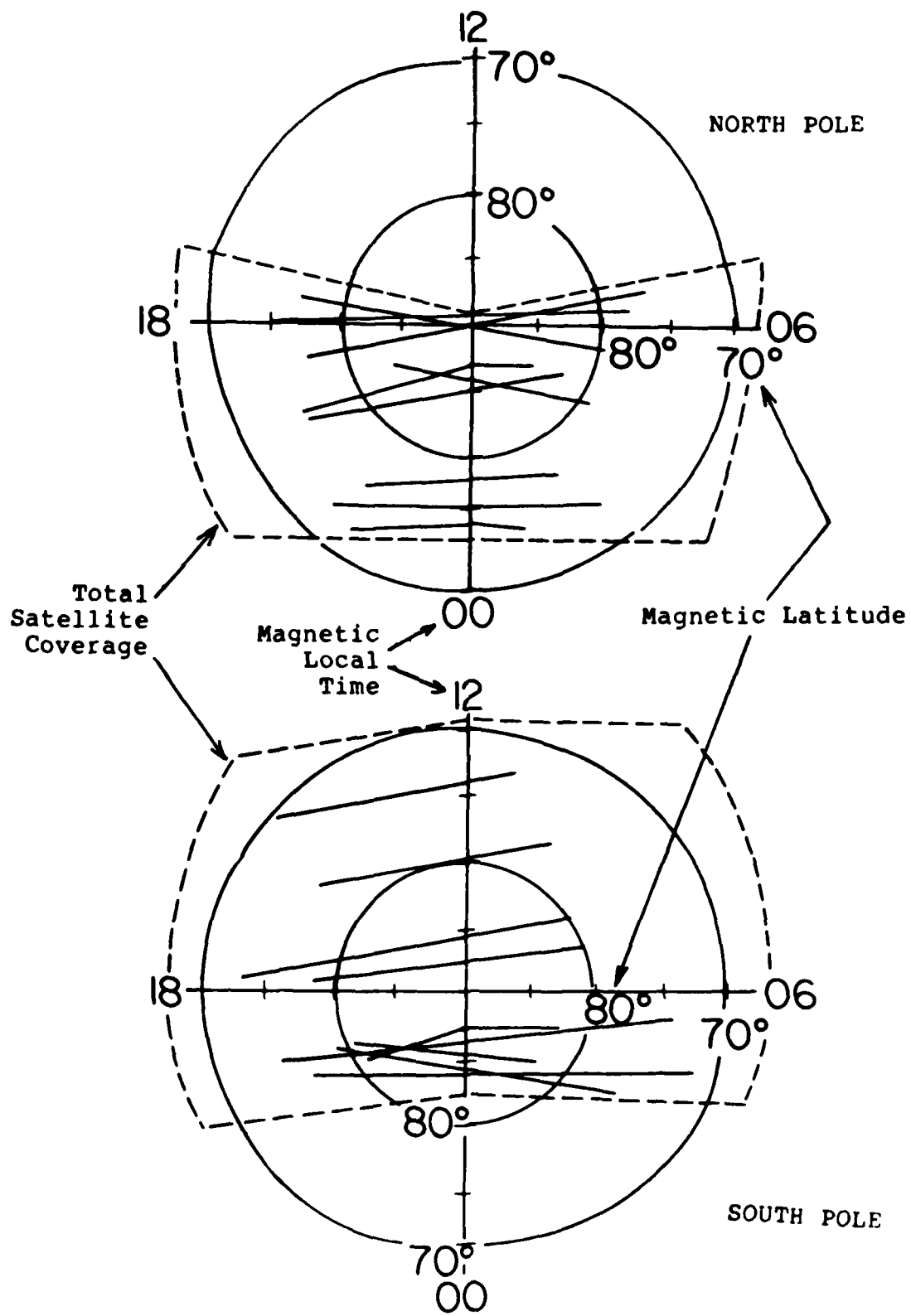


Figure 5a
 Sample DMSP-F6 Trajectories
 January, 1983

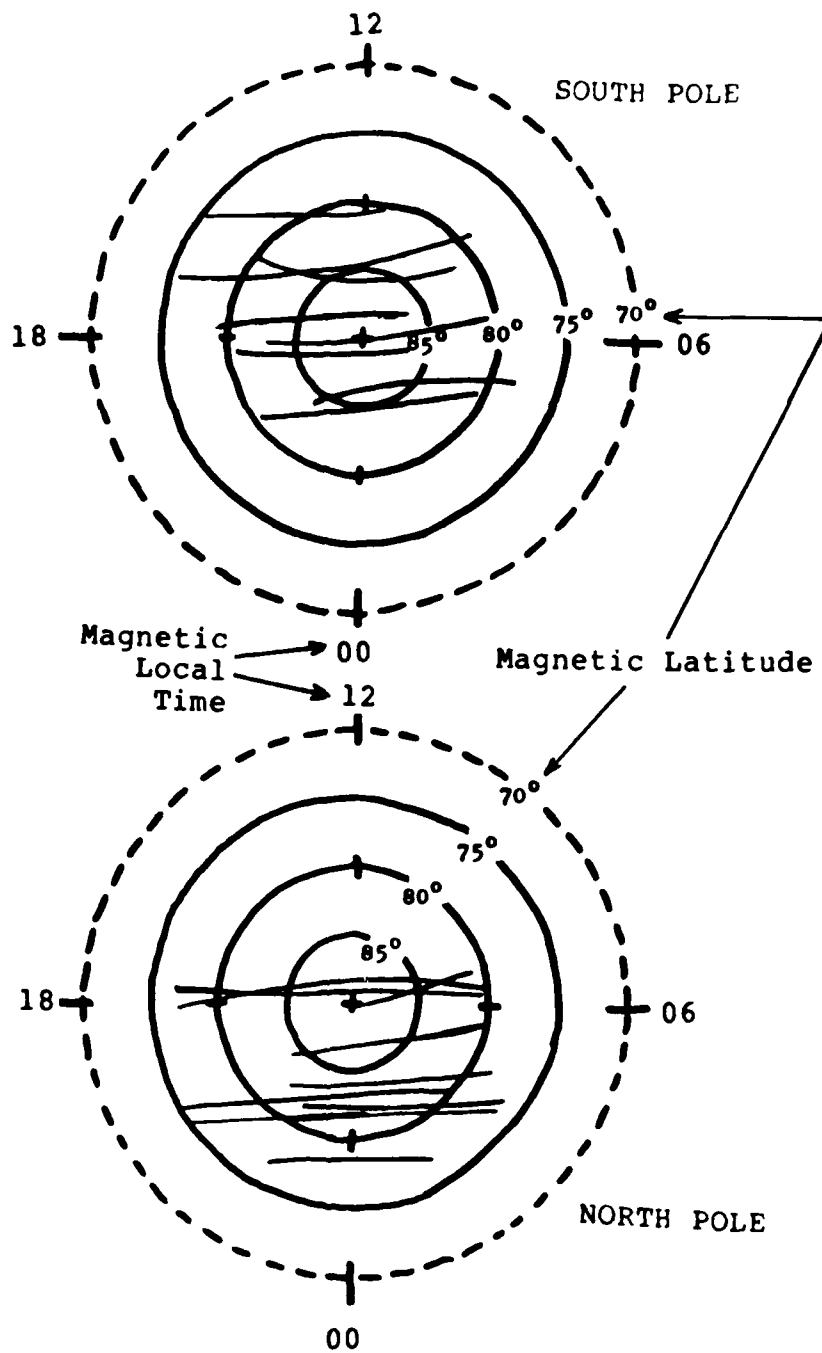


Figure 5b
 Sample DMSP-F6 Trajectories
 May/June, 1983

time period (~hours). There is no substantial difference between the winter and late spring trajectories. The orbital period of the satellite is 101 minutes, resulting in the satellite travelling ~ 725 m during the access of one channel (98 ms) and ~7.3 km during one spectrum of data (1 second).

V. DATA ANALYSIS

Selection

Data was surveyed from archive microfiche for the period spanning January to June, 1983. The polar rain is defined as the smoothly continuous electron precipitation above the auroral oval having average energies of ~ 100 eV and integral energy fluxes of $\sim 6 \times 10^5 - 7 \times 10^6$ keV/cm²-s-sr. Electron intensities in the polar rain are very weak by space physics standards (Yeager and Frank, 1976:3966). Therefore, polar rain data must be averaged over a long time period (~ 30 s minimum) to achieve statistically meaningful results. This is especially true in the higher energy (>1 keV) range, where only a fraction of count is seen (on average) per second. The uniformity of the polar rain makes the averaging technique valid (Gussenhoven and others, 1984:9786). A relatively long event criteria of 3 1/2 minutes of consecutive polar rain was established for this study; a shorter event could still provide valid statistics, but was not considered here. Events were chosen only when IMF and/or solar wind data were available.

A typical DMSP-F6 satellite pass exhibiting polar rain is shown in fig 6. The figure plots, from top to bottom, the average electron energy (keV), the integral (for $E > 32$ eV) energy flux (keV/cm²-s-sr) and the integral number flux (electrons/cm²-s-sr). The horizontal axis represents time, with each hash mark equal to one minute in universal time.

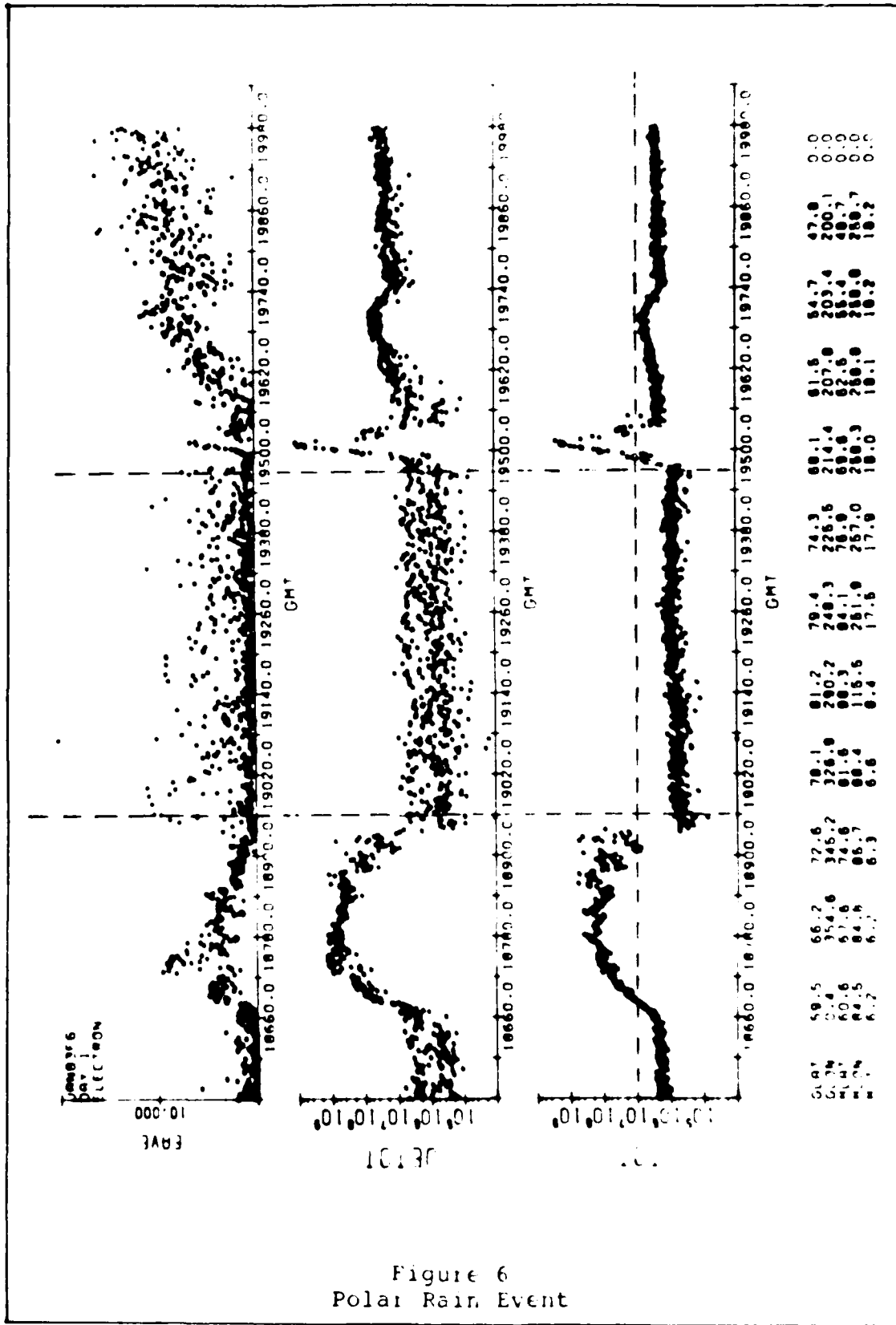


Figure 6
Polar Rain Event

The bottom of the figure is annotated with the geographic latitude (GLAT) and longitude (GLON), the geomagnetic latitude (MLAT) and longitude (MLON), and the magnetic local time (MLT). All are mapped down the magnetic field line to an altitude of 110 km (Hardy and others, 1984a:28). The negative latitudes indicate this example is a south pole pass. The area between the dashed lines is the polar rain. This example (as did most) exhibits some noise contamination, which is seen in the large fluctuations in average energy (EAVE).

Processing

Altogether, over 275 passes over the northern and southern poles met the criteria of having both polar rain and interplanetary data. Utilizing SSJ/4 data on magnetic tapes provided by the Air Force Geophysics Laboratory, the polar rain intervals were analyzed. As mentioned above, the count rates must be averaged over long intervals to obtain valid statistics. For the initial portion of this study, an averaging interval of 60 s was chosen. This was done to allow comparison with the data in Riehl and Hardy (1986), who used a 45 s interval, and resulted in 3-7 averaging intervals for most satellite passes.

The conversion from raw count rate to either differential integral flux ($e^-/cm^2\text{-keV-s-sr}$) or values of the distribution function (sec^3/cm^6) is detailed in Appendix A.

In summary,

$$f_i(\vec{r}, E_i) = \frac{m^2 C_i / \tau}{2 E_i G_i}$$

where

f_i = value of the distribution function for the
i-th channel

E_i = energy of the i-th channel

C_i = count rate of the i-th channel

G_i = energy independent geometric factor of the
i-th channel

τ = access time (98 ms) of the channel

Since the distribution function describes the probability of finding an electron with a given energy at a given location, it is the most accurate way to describe the electron precipitation. But it is more convenient to assign temperatures and densities to describe the precipitation, especially since it is known to be nearly maxwellian.

Since a maxwellian distribution may be written

$$f(\vec{r}, E) = n_0 \left(\frac{m}{2\pi kT} \right)^{3/2} \exp^{-E/kT},$$

the natural logarithm may be taken on both sides to show

$$\ln[f(\vec{r}, E)] = -E/kT + \ln[n_0 (m/2\pi kT)^{3/2}].$$

It is seen that the natural log of the distribution function is proportional to the energy, with the slope being the negative inverse of the temperature and the intercept being a function of temperature and density. Matching straight lines to the maxwellian portions of the distribution function will generate the temperature and density of the distribution. But before values of the distribution function can be calculated, the count rates (C_i) must be corrected for background and instrumental noise.

Noise Sources

The background noise is caused by cosmic rays (primarily high energy protons) which penetrate the instrument housing and cause spurious counts when colliding with the channeltron. Since the SSJ/4 has no background channel, an assumption must be made to treat this natural background. Previous studies (Gussenhoven and others, 1984:9788; Riehl and Hardy, 1986:1558) have assumed all counts in the highest energy channel (30 keV here) are background counts. This is clearly a conservative assumption, since a finite number of high energy electrons do exist.

This study used a technique which involved the ten highest energy channels to determine the natural background. An initial guess was made for the background and a weighted least-squares fit (Bevington, 1969:92-133) was made on channels 1 (30 keV) through 10 (984 eV). Channels 1-10 were used because that range was seen to be a common grouping for the high energy fit in test runs. The fit predicted a "true" count rate for the 30 keV channel, and a new background guess is formed. The process continues until convergence between the prediction and the fit is achieved. This iterative technique meant the assumed background is always less than or equal to the 30 keV count rate.

Electrostatic analyzers rarely have instrumental noise. Unfortunately, two problems with the SSJ/4 sensor flown on DMSP-F6 were previously documented (Hardy and others, 1984a)

and during this study two additional, possibly related, problems were noted. The previously documented problems were anomalously low count rates in the three lowest energy channels (32,46,68 eV) and detection efficiency of the entire low energy (32 eV - 992 eV) analyzer. It was hypothesized that the decrease in detection efficiency is the result of hydrocarbon contamination of the channeltron. Corrections to both problems have been developed (Hardy and others, 1984a:47-50).

This study noted specific anomalies in channels 1, 2, 11, and 12. A sample summation of a polar rain interval is shown in Table III. Although count rates for all other channels range from 0.15 to 1.07 per second, it is seen the noted channels' count rate is well above their neighboring channels. Perhaps even more graphic evidence that channels 1, 2, 11, and 12 are noisy is indicated in parentheses after the count rate; the number is the ratio of the raw count rate listed in Table III to a the perfect bi-maxwellian listed in Table A (the same polar rain interval). Most of the ratios are near 1.0 (indicating a nearly perfect double maxwellian distribution), and only channels 1, 2, 11, and 12 are above 4.5. The high ratios in channels 9 and 10 are a result of the raw count rate being uncorrected for the natural background.

Channels 11 and 12 had to be corrected for instrumental noise in every polar rain event analyzed. Channels 1 and 2

required instrumental corrections for about 80% of the events. Channels 1 and 2 were the most difficult to correct, because they are end points to the data set. Channels 11 and 12 (see fig B) could be compared to their adjacent (and cleaner) channels. The specific corrections chosen for this study are discussed in Appendix B.

Some key points should be made regarding the noise corrections. Any correction to the 30 keV channel is especially critical since this channel establishes the background noise as discussed above. It was noted in test runs that various instrumental noise corrections had a wide variation of impacts on the background noise correction.

Also, since it is known (see Appendix B) that the ratio of channel 10 to channel 11 should be 3.3, it is interesting to note that Hardy and others (1984a) saw ratios >3.3 while fig 5a indicates ratios <3.3 for the polar rain. The polar rain data cannot be attributed to an efficiency problem, since the polar rain data indicates too many counts (not too little, as expected) in the low energy analyzer (at least for channels 11 and 12). Noting the noise is in the two highest energy channels (voltages) in each curved plate analyzer, it is suspected high voltage ripple is causing spurious counts. Since the data of Hardy and others is based on much higher count rates than seen in the polar rain, it may be there is actually a combination of problems within the sensor.

TABLE III

Sample Polar Rain Interval
from March 16, 1983

<u>Channel</u>	<u>Energy</u>	<u>Count Rate*</u>	(Ratio to Table A)
1	30180 eV	.51	(38.)
2	20620	.55	(7.7)
3	14040	.28	(1.5)
4	9580	.22	(.8)
5	6500	.26	(.8)
6	4420	.21	(1.1)
7	3050	.23	(1.1)
8	2060	.25	(1.8)
9	1410	.29	(3.5)
10	984	.24	(4.4)
11	992	.67	(40.)
12	679	.43	(11.)
13	462	.35	(1.4)
14	317	.78	(1.1)
15	213	1.07	(.9)
16	145	1.07	(.9)
17	100	.78	(.9)
18	68	.54	(1.1)
19	46	.24	(1.0)
20	32	.15	(1.4)

* uncorrected for noise sources

A pictorial summary of the effect of the noise corrections on values of the distribution function is shown in fig 7. In the figure, the x's indicate uncorrected data and the o's indicate the final corrected form of the data. Note that channels 13-17 were nearly noise free. Also note the major noise correction that was performed on channels 1, 2, and 12. Channel 11 was uncorrectable for this case. The dashed line indicates the level of a single count over the averaging interval.

After all channels are corrected for instrumental and background noise, the distribution functions were fit by a single or double maxwellian. Fits were performed using straight linear regression, calculating the high energy component first (if it existed) and subtracting it from the low energy component. For cases where the double maxwellian fit was appropriate, the number of channels included in the low energy and high energy maxwellians were varied to achieve the best fit to the shape of the distribution function. This was done by stepping through all combinations which contained a minimum of four data points (i.e., chan 1-4 [high] and chan 5-20 [low]; chan 1-5 and chan 6-20; . . .; chan 1-16 and chan 17-20). The "best" fit was determined through evaluation of the correlation coefficients and the variances on the slopes and intercepts of the linear fits.

An example of this process is reproduced in Table IV for a single maxwellian case. The channel range indicates

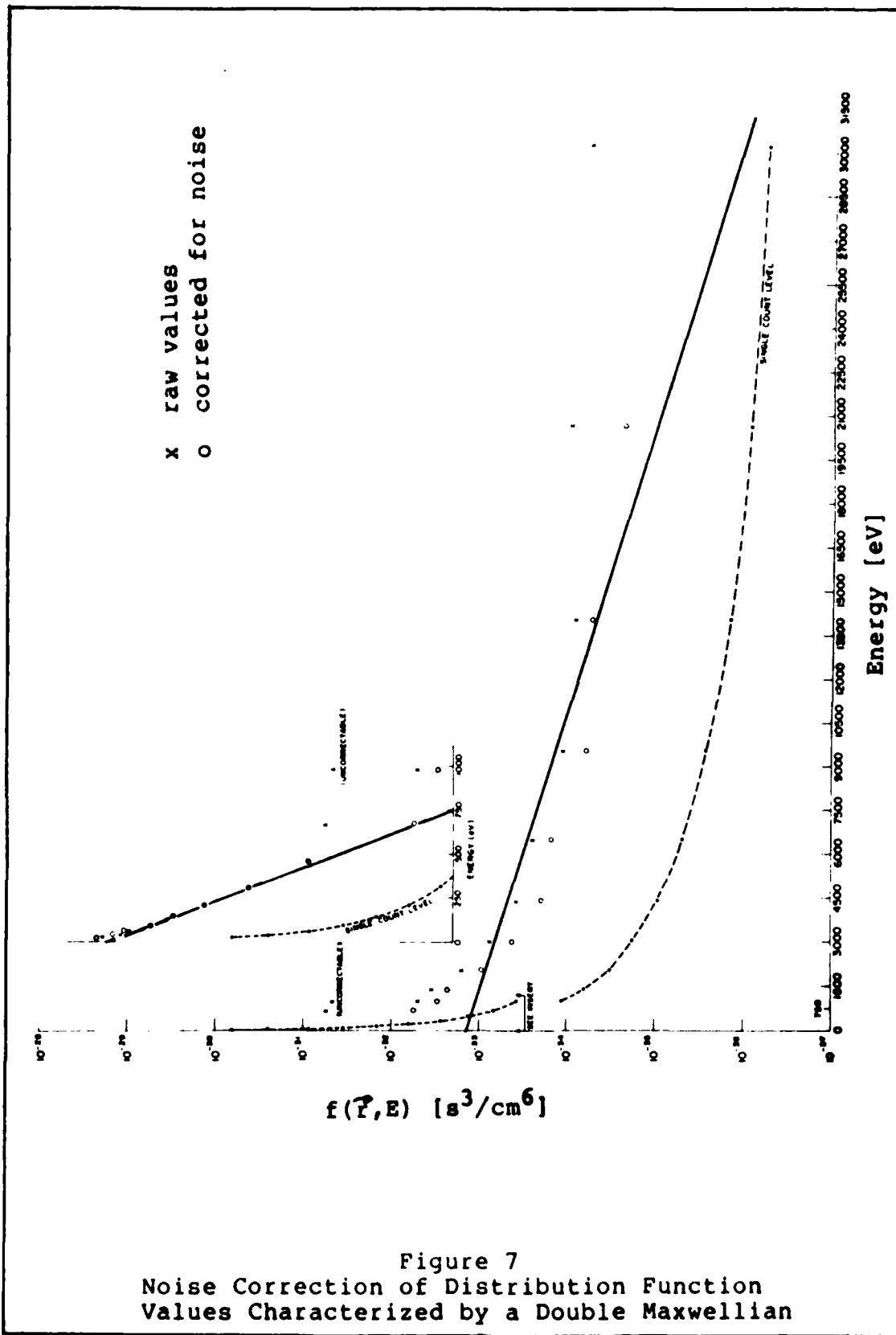


Figure 7
 Noise Correction of Distribution Function
 Values Characterized by a Double Maxwellian

TABLE IV

Fitting Process for a Single Maxwellian

<u>Channel Range</u>	<u>Temperature (eV)</u>	<u>Density (cm⁻³)</u>	<u>Correlation Coefficient</u>
9-20	128.5(23.9)	0.018(0.011)	-0.957(1x10 ⁻⁶)
10-20	119.0(24.0)	0.018(0.011)	-0.958(3x10 ⁻⁶)
11-20	109.4(27.1)	0.018(0.012)	-0.945(4x10 ⁻⁵)
12-20	81.5(22.3)	0.019(0.015)	-0.988(7x10 ⁻⁷)
13-20	79.4(23.7)	0.020(0.016)	-0.987(6x10 ⁻⁶)
14-20	69.5(26.1)	0.020(0.019)	-0.994(6x10 ⁻⁶)
15-20	63.3(33.6)	0.021(0.024)	-0.994(5x10 ⁻⁵)
16-20	56.5(47.1)	0.020(0.032)	-0.994(5x10 ⁻⁴)
17-20	51.5(76.6)	0.020(0.045)	-0.988(1x10 ⁻²)

the channels that were inclusive in the fit. The number in parentheses after the temperature and density is the error, which is calculated from the variance in the slope and intercept associated with the linear fit. The error will tend to increase (as exhibited in the Table) when fitting less data points because the number of degrees of freedom (defined for a linear fit as two less than the number of points being fit) is reduced. On the other hand, less degrees of freedom tends to make the correlation coefficient increase.

One must proceed cautiously in using the correlation coefficient to determine the best fit when there is a small (and rapidly changing) number of degrees of freedom; naively

using the highest correlation coefficient would result in the selection of the 69.5 eV, 63.3 eV, or 56.5 eV fit as the most linear (closest to maxwellian). But the correlation coefficient is just a measure of goodness of fit which is highly dependent on the number of degrees of freedom, and is inappropriate to judge the most linear fit with this data.

The true measure of the best fit is which fitting combination had the lowest probability that an uncorrelated set of the same number of data points would achieve a better correlation coefficient than the fitting combination did (see Bevington, 1969:310-312). This probability is annotated in parentheses after the correlation coefficient, and clearly shows the 81.5 eV (channels 12-20) is the best fit (with only a 1.4 in 10^6 chance that nine uncorrelated data points would achieve a correlation coefficient better than 0.988). This is clearly a linear fit; the distribution is highly maxwellian.

An example of fitting a double maxwellian to the data is displayed by the straight lines in fig 7. When two components were seen, the best fit was generally chosen by comparing the product of the fitting probabilities of each component. If different fitting combinations had similar probability products, the combination with the lowest overall error associated with the temperatures and densities was selected. The case exhibited in fig 7 resulted in $kT_{low}=81$ eV, $n_{low}=0.0175$ cm⁻³, with a correlation coefficient of

-0.994 and a corresponding probability of 6×10^{-8} (highly maxwellian). The high energy component had $kT_{\text{high}} = 4300$ eV, $n_{\text{high}} = 0.00046 \text{ cm}^{-3}$, a correlation coefficient of -0.92 and a probability of 6×10^{-5} .

The probability associated with fitting the high energy component was generally worse than the low energy component, with values as high as 10^{-2} . This indicates the high energy component is not as maxwellian as the low energy component. The practice of associating a temperature and density with the high energy distribution function values is used in this study as the method to compare different polar rain events. The reader should not take the use of temperatures and densities as implying the high energy component is always maxwellian.

Two data sets were constructed using the analysis techniques discussed in this Section. The first data set used medium length (60 s) averaging intervals and included all types of flux gradients. This was a "test" data set used to evaluate whether the noise correction techniques yielded polar rain characteristics similar to those discussed in Section III. The second data set used very long (100's of seconds) averaging intervals and only events where the flux gradient was constant across the polar cap.

VI. RESULTS AND DISCUSSION

A limited data set was created from 87 polar rain events in January and February, 1983, using 60 s averaging intervals. This resulted in 450 such intervals (an average of ~5 per event). Of these, 80% were best fit by a double maxwellian. The low energy component had an average temperature of 82 eV, but a relatively large statistical variation. This average temperature is in agreement with the 80 eV obtained by Riehl and Hardy (1986) using a different detector system and the conservative background assumption. The high energy component was not in such agreement; it varied from a few hundred eV to 6.5 keV.

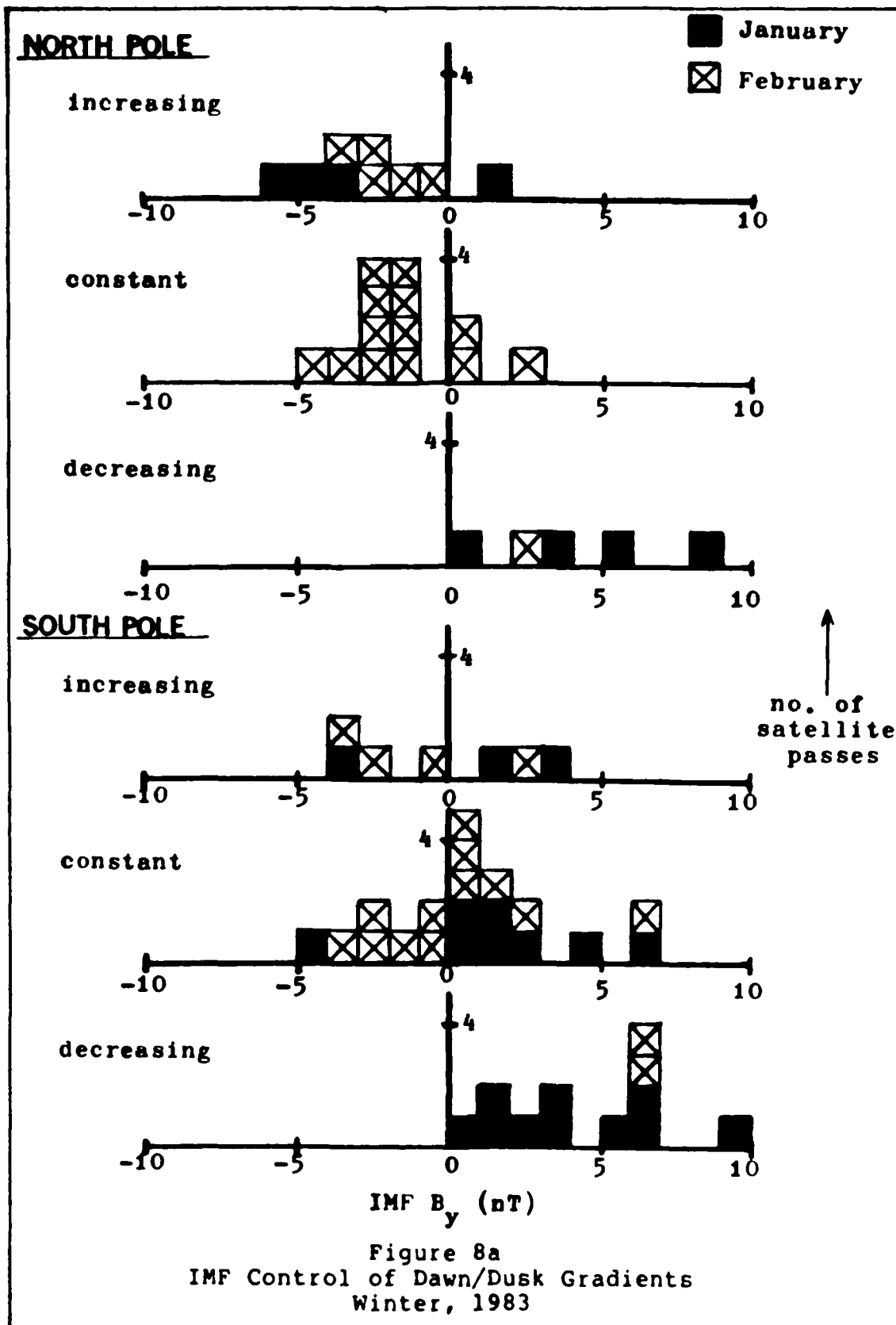
Integral flux values were also similar to those seen by Riehl and Hardy (1986); an average integral flux of 2.3×10^6 e^-/cm^2-s-sr was obtained. The flux distribution was skewed, with a tail to the high flux side. The density of the low energy component was 0.03 cm^{-3} (comparable to densities noted in Section III, but 80% lower than Riehl and Hardy, 1986). The average density of the high energy component was 0.0046 cm^{-3} , considerably higher than the typical value reported earlier. The large difference in density of the high energy component is likely a result of the less conservative natural background assumption used in this study.

This test data set showed the low energy component has consistent characteristics regardless of fitting technique, while the high energy component is very sensitive, both to

averaging interval length and to background assumption. It also showed the noise corrections used did not generate unreasonable or inconsistent (such as producing high energy component temperatures greater than the assumption--see Appendix B, Step A) results. Based upon this, the noise corrections were deemed acceptable.

Since the gradient information was available, the IMF B_y control of dawn/dusk flux gradients was examined for the winter (January and February) and the late spring (May and June). Only three flux gradients were considered: linearly increasing, linearly decreasing, and constant across the cap. Gradients which had a peak at the center of the cap ("concave down"), a minimum at the center of the cap ("concave up"), or some other unusual gradient were not used. Figure 8 shows how B_y controlled the gradients. The vertical axes indicate the number of events for each 1 nT bin of B_y . The noted gradients are along satellite trajectory (dawn to dusk in the north pole and dusk to dawn in the south pole). Displayed in this manner, the open magnetosphere theory predicts the gradient should increase when $B_y > 0$ and decrease when $B_y < 0$. In reality, there is a gray area near $B_y = 0$ such that there is either no gradient, or it cannot be resolved.

There is excellent agreement with theory. Of the cases with a gradient, nearly 85% agreed with the predicted gradient. The few cases in disagreement did not result from a



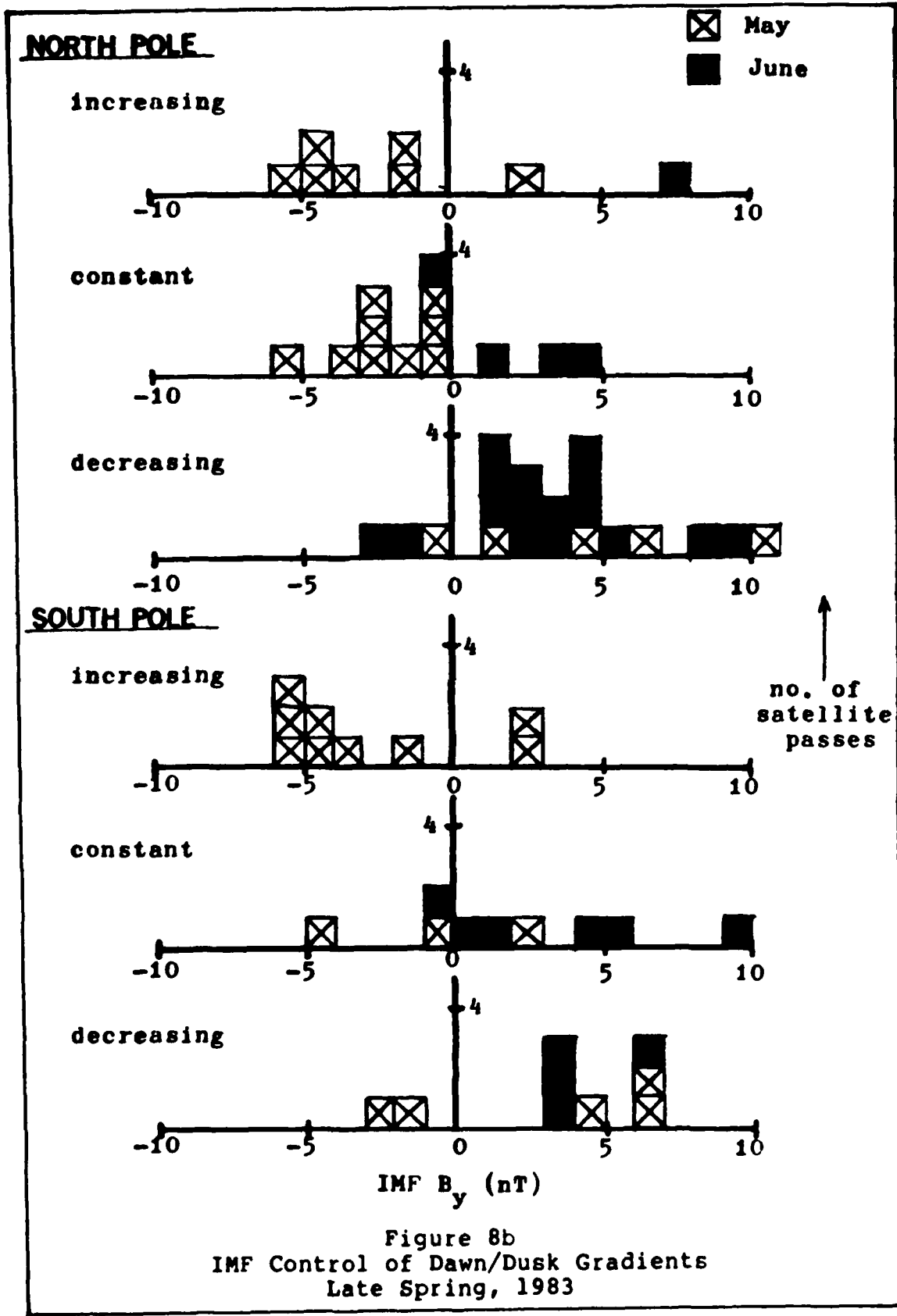


Figure 8b
IMF Control of Dawn/Dusk Gradients
Late Spring, 1983

particular month or season. There was slightly better agreement with theory in the winter (88%, compared to 81% for the late spring), but the difference is less than the statistical error. Figure 8 indicates there is no seasonal variation associated with the polar rain flux gradients.

The outstanding agreement was somewhat surprising after noting the results in the southern hemisphere from Riehl and Hardy (1986). A closer examination of their data set revealed a possible explanation. They used data from the DMSP-F2 satellite which was launched into a nearly dawn/dusk orbit; it was actually launched in the 0700-1900 meridian plane. A review of sample satellite trajectories shows the south pole precession moves the satellite even more off the dawn-dusk meridian, forcing it to cut an angle across the dominant noon-midnight gradient noted by Gussenhoven and others (1984). This resulted in increasing dusk to dawn gradients (equivalently reported by Riehl and Hardy as decreasing dawn to dusk) being seen consistently.

To pursue the strahl source theory, a second data set was constructed. Events were constrained to have no gradient, since variations in the average energy associated with the gradients (Gussenhoven and others, 1984) were to be avoided. One hundred seventeen (out of 192) events met the gradient criteria. The averaging was performed over the entire event, resulting in averaging intervals of 210-550 seconds. The desired outcome was achieved; the fitting

process showed the high energy component to be more consistent. Only 9 of the 117 events (8%) had no high energy component.

Two interesting points were raised while constraining the data set to constant gradients. It was noted that $B_z > 0$ was generally associated with a flux gradient. In fact, there was a gradient in nearly 6 out of every 10 events (56%) when B_z was positive. But only 39% of all events (independent of the orientation of B_z) had a gradient. This would suggest B_z plays a role in determining the preferential east/west entry of the polar rain. It was also noted the flux constraint generally eliminated the preferred cap associated with IMF sector. Twenty seven events (23%) had no IMF data available, but for those that did only 32% (29 events) were in the preferred cap. This is reduced from the ~47% of the events that were in the preferred cap before the gradient constraint. Having constant flux gradient events occurring more often in the unpreferred cap may be a result of the enhanced flux in the preferred cap making it easier to resolve a gradient.

Figure 9 shows the temperatures which resulted from this data set. It is seen the low energy component is well characterized as ~80-90 eV. The average temperature was actually 87 eV. The high energy component, although still having a wide range of values, shows a prominent peak between 3600 and 4800 eV. Note the error bars on the low

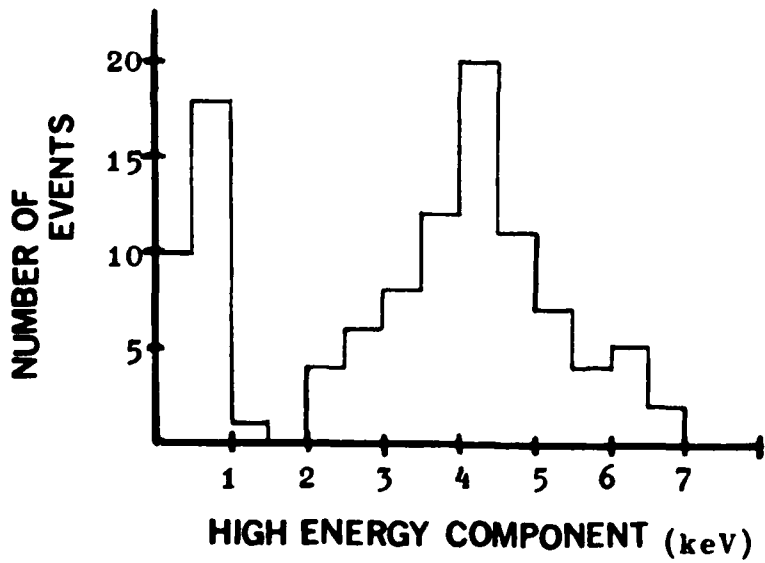
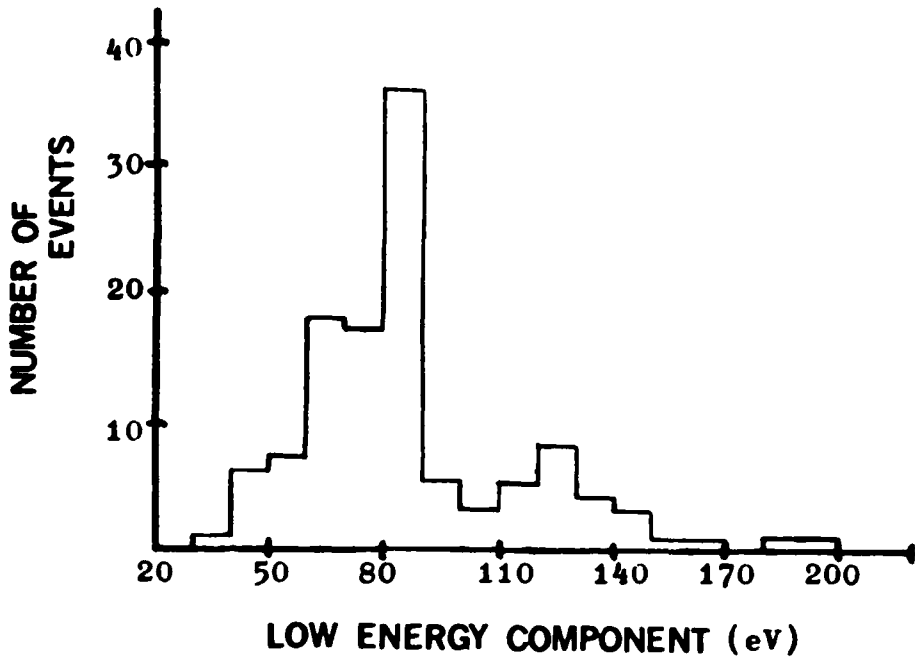


Figure 9
Polar Rain Temperatures

energy temperature are ~25%, while the high energy temperature usually has an error of ~40%-75%. The average densities were 0.023 cm^{-3} and 0.0027 cm^{-3} for the low and high energy components, respectively. The characteristics of the low energy component strongly match those of the strahl, suggesting the polar rain is of strahl origin.

With the established data set, correlations were attempted with solar wind (temperature, density, and velocity) and IMF (B_x , B_y , and B_z) parameters. To allow for the delay between the IMF measurements and when IMF fluctuations affect precipitations at the earth's polar caps, a 45 minute delay time was assumed. This delay time has been reported by Baker and others (1981) for a different type of precipitation which originates in the magnetotail, but should apply equally well to the polar rain.

Since the low energy component temperature is so stable, it did not correlate with any solar wind parameters. This was the case in both preferred and unpreferred caps. Figure 10 shows the low energy component temperature plotted against the solar wind velocity. There is clearly no correlation, either for all events (fig 10a) or in the preferred cap (fig 10b). The lack of correlation with the high speed solar streams, as predicted by Fairfield and Scudder (1985), was disappointing.

There were three promising results seen. Two of these are displayed in figures 11 and 12. Figure 11 shows the

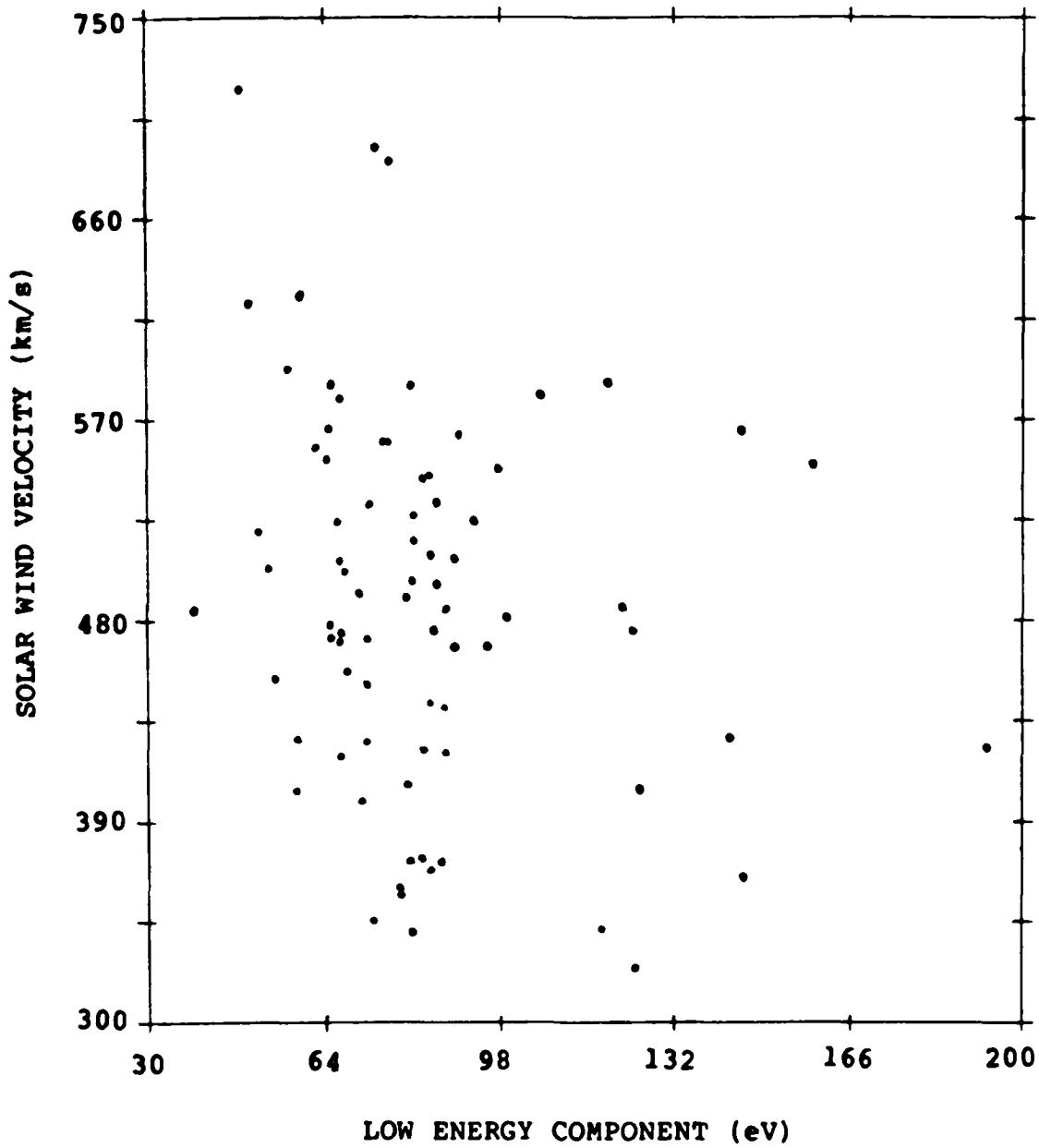


Figure 10a
 Solar Wind Velocity Versus Polar Rain Temperature
 All Cases

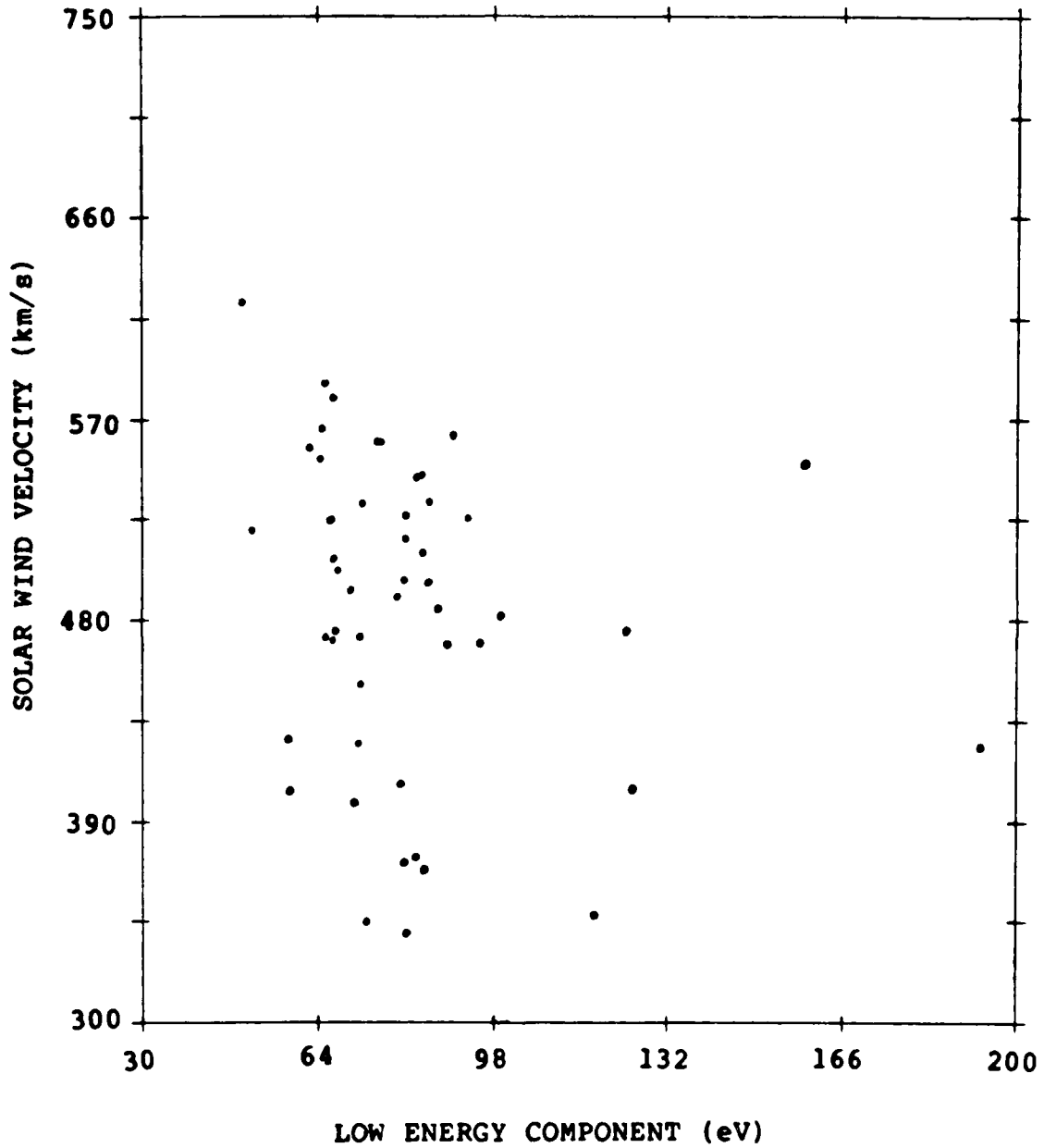


Figure 10b
 Solar Wind Velocity Versus Polar Rain Temperature
 Preferred Cap

relationship between the integral flux and B_x (fig 11a), and integral flux and B_y (fig 11b). These plots were created by reversing the sign of B_x in the south pole, and B_y in the north pole, to align the preferred and unpreferred caps in the same plot. The integral flux was averaged into 1 nT bins, with the error bar indicating the statistical variation within each bin. The number of events found in each 1 nT bin is indicated at the top of the plot. It is seen that, with the exception of the -2 nT to 0 nT bins, the integral flux increases with B_x . The increase in integral flux is even more obvious with respect to B_y . Since both plots put the preferred cap on the right, the increases are consistent with the open magnetospheric model.

Figure 12 depicts the solar wind density versus the density of the low energy component. Figure 12a shows all cases, and it is seen that there is some evidence of the inverse relationship proposed by Fairfield and Scudder (1985). But there are many unexplained cases which have a low solar wind density and a low polar rain density. Figure 12b depicts the relationship in the preferred cap. It is seen that ~85% of the unexplained cases occur in the unpreferred cap. The remaining unexplained cases may be attributed to the fact that the polar rain density is essentially plotted against the core density. The bulk of the solar wind density is attributed to the core. The core density and the strahl density should be proportional, but a

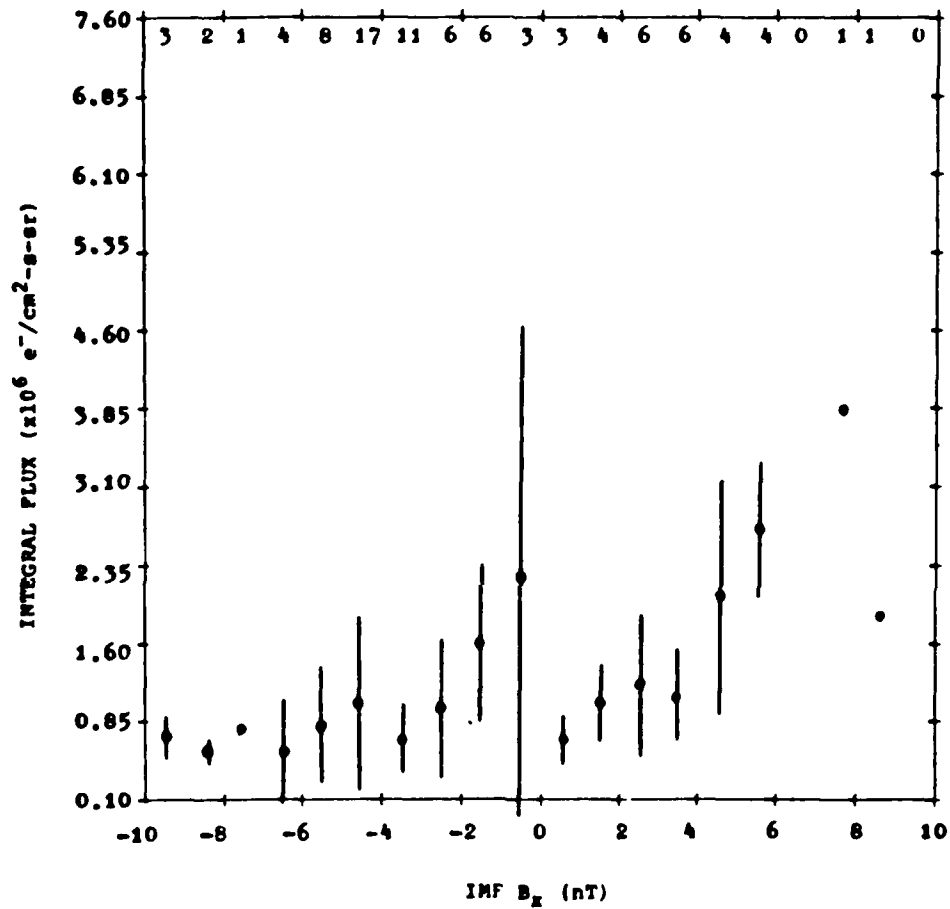


Figure 11a
 Integral Flux Versus IMF Components
 B_x

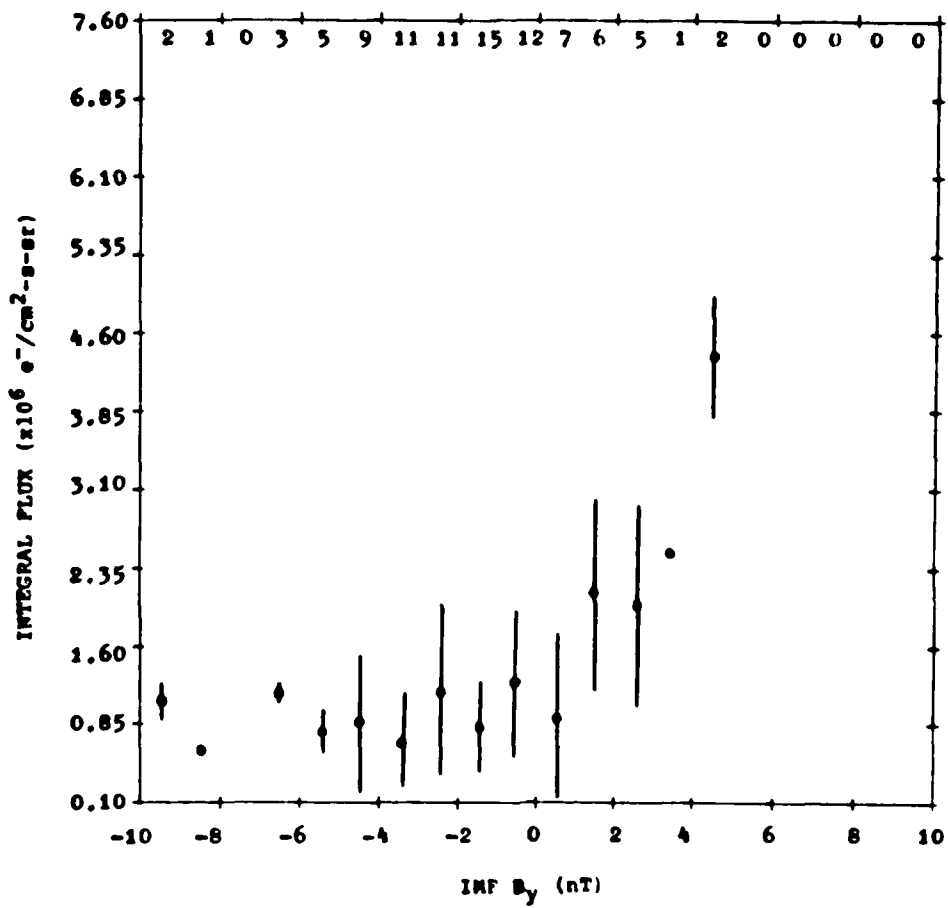


Figure 11b
 Integral Flux Versus IMF Components
 B_y

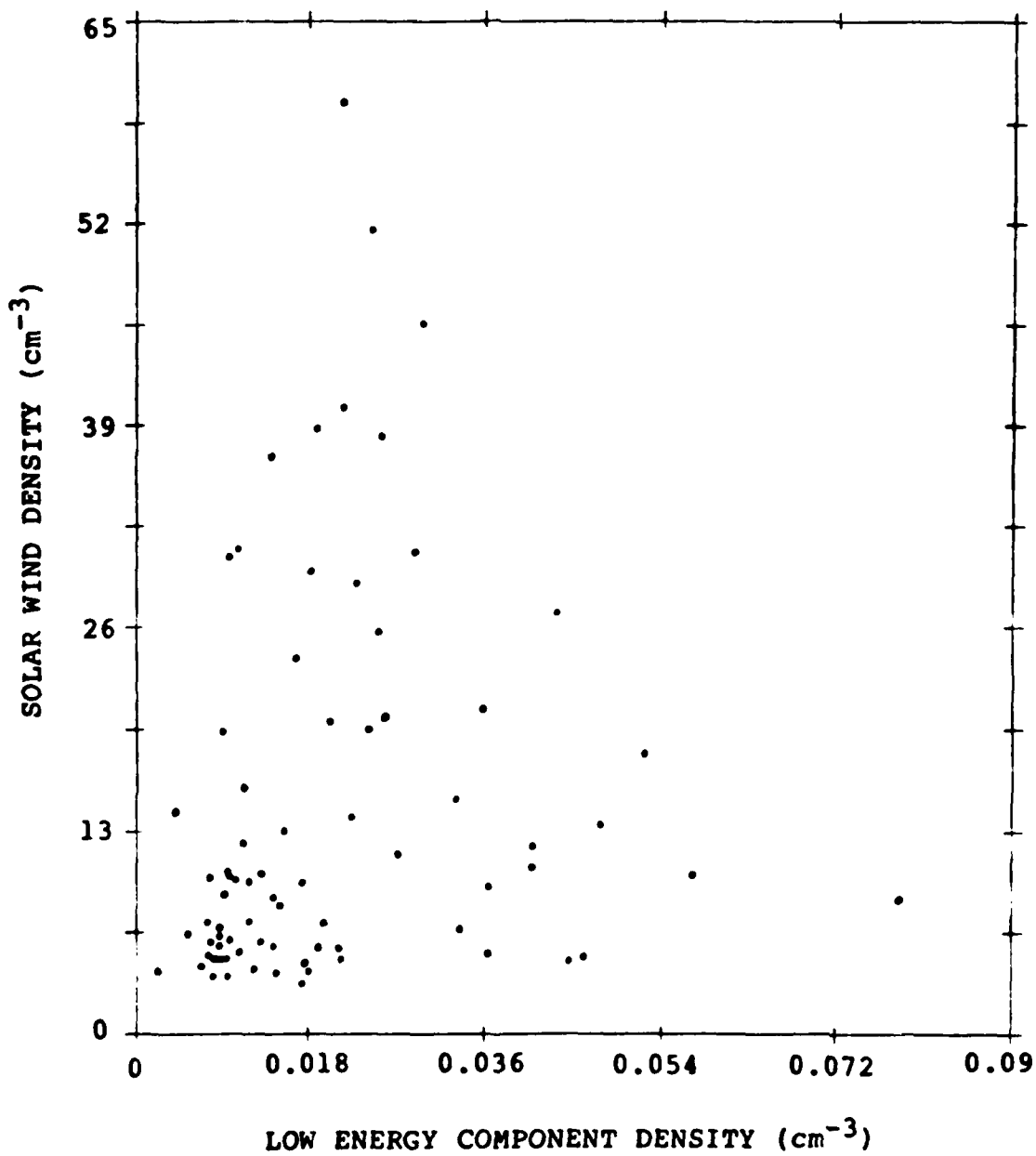


Figure 12a
 Solar Wind Density Versus Polar Rain Density
 All Cases

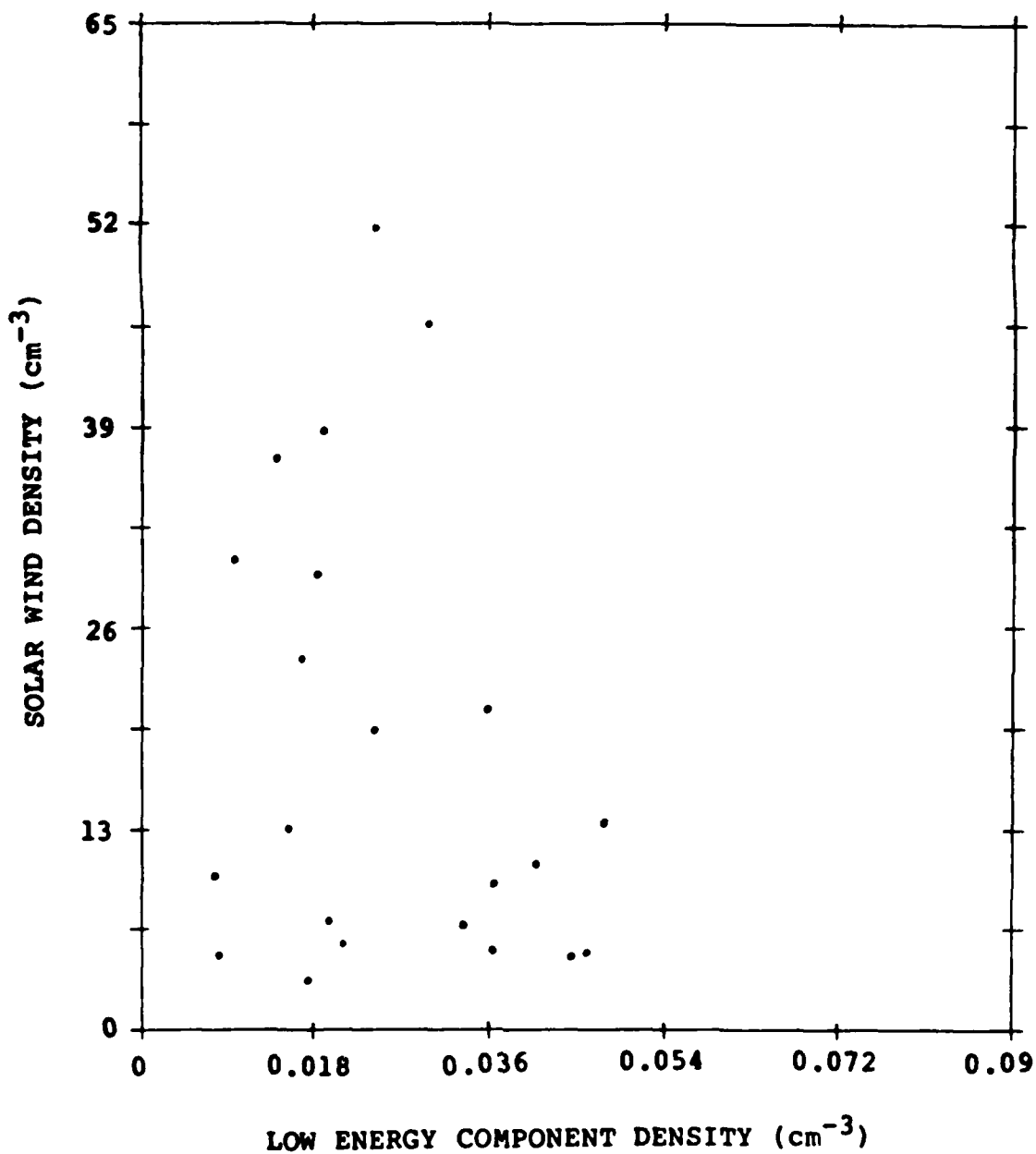


Figure 12b
Solar Wind Density Versus Polar Rain Density
Preferred Cap

better inverse relationship might be established if the strahl density (which, unfortunately, is not available) were plotted versus polar rain density.

Finally, the high energy component was examined with respect to IMF sector structure. In the preferred cap, ~75% of the events had a temperature greater than 2.2 keV. But in the unpreferred cap, there was also a large percentage of events above 2 keV. Fairfield and Scudder (1985) predicted a hotter component in the preferred cap (as seen here), but said no high energy component should be seen in the unpreferred cap. Unfortunately, this was not the case.

Considering the low densities of the high energy component, it may be likely it originates within the magnetosphere. The plasma sheet is known to have a wealth of high energy electrons. A small diffusion rate or scattering rate may account for some (all?) of the high energy electrons.

The nature of the high energy component with respect to the low energy component accounts for the gradients in average energy reported by Gussenhoven and others (1984). Since the average energy is a weighted average over all electrons, an increase in integral flux (which is dominated by the lower energy electrons) lowers the average energy. On the nightside, there are less lower energy electrons, so the average energy is higher.

When the fitting was done to the Maxwellian distributions, it was implicitly assumed the distribution was iso-

tropic, since the 3-dimensional velocity distribution was used. Yet the SSJ/4 effectively looks in only one direction (measures the 1-D velocity distribution). Heikkila and Winningham (1974:4) have reported the low altitude polar rain to be isotropic, experimentally validating the implicit assumption. But it is perhaps more convincing to map the deep tail electron distribution to lower altitudes to verify both the isotropy and the bi-directionality reported earlier.

Magnetic field models (Malcolm, 1986) indicate the field intensity at 800 km varies from 0.39-0.41 gauss over a polar rain event. The models also project a magnetic field of ~ 170 nT on an open field line in the northern tail at a distance of $5.6 R_e$ from the earth. It has been reported (Slavin and others, 1983:975) that the field intensity is ~ 9 nT in the deep tail ($\sim 220 R_e$). Conserving the first adiabatic invariant, Table V shows how different pitch angles vary as the electrons move into a region of stronger magnetic field.

It is clearly seen that only field aligned electrons originating in either the deep or near tail will be detected by the SSJ/4 sensor. Electrons with pitch angles greater than 0.85° (3.7°) in the deep (near) tail will mirror at altitudes higher than DMSP-F6. These simple calculations support the isotropy noted by Heikkila and Winningham (1974) and that noted by Yeager and Frank (1976) in the near tail.

TABLE V

Pitch Angle Mapping the Deep Tail Electron
Distribution to Lower Altitudes

From	<u>220 R_e</u>	to	<u>5.6 R_e</u>
	0°		0°
	1°		2.2°
	2°		4.4°
	4°		8.7°
	6°		27.0°
	8°		37.2°
	10°		49.0°
	12°		64.6°
	13.3°		mirrors

From	<u>5.6 R_e</u>	to	<u>800 km</u>
	0°		0°
	0.25°		3.9°
	0.5°		7.8°
	0.75°		11.7°
	1°		15.7°
	1.25°		19.8°
	1.5°		24°
	2°		32.8°
	2.5°		42.6°
	3°		54.4°
	3.5°		71.5°
	3.7°		mirrors

And since the loss cone is so small, wider angle detectors (Baker and others, 1986, had ~20° resolution) will easily detect the mirrored electrons streaming away from the earth. But this raises the interesting question why Baker and others saw uni-directional streaming in the unpreferred cap. It has been reported here the the polar rain temperature (low energy component) is generally the same in the preferred and unpreferred caps. If the strahl is the polar rain source, why is it seen in the cap connected to the heliosphere? Also, strahl electrons would have to be ex-

tremely field aligned (entirely in the loss cone) in the
unpreferred cap to account for Baker and others' data. If
the strahl is so field aligned, why so?

VII. SUGGESTIONS AND RECOMMENDATIONS

There are many questions which remain to be answered on the interaction process between the solar wind and the magnetosphere. The IMF Z-component plays a key role in the nature of particle precipitations, yet variations in B_z are poorly understood. It is not clear why $B_z < 0$ is noted to be the dominant condition during the polar rain, yet particle data seen in the magnetotail has not seen such a dependence (Yeager and Frank, 1976; Fairfield and Scudder, 1985; Baker and others, 1986). An especially large question looms as to the character of solar wind (strahl) on field lines connecting to the unpreferred cap.

It is felt the iterative technique to handle the natural background is effective, although instrumental noise made that task less routine in this study. The long averaging intervals improved the fitting consistency; they are recommended. Future sensors flying on upcoming DMSP flights will, hopefully, return cleaner data. Too much effort went into handling the noise and this limited the number of polar rain events which could be analyzed. Ideally, at least 200 intervals are necessary to really break the data out by pole and IMF sector. In addition, a finite number of events will be lost due to lack of IMF or solar wind data.

There is a possibility that IMF correlations would improve if less than hourly averages were used. Future researchers may want to obtain a magnetic data tape from the

World Data Center containing shorter averaging intervals. This would also apply the solar wind correlations.

Many of the recent reports deal with the anisotropy of the electron distributions. Because DMSP is a non-spinning satellite, the SSJ/4 detector cannot determine pitch angle information. It would be useful to obtain low altitude pitch angle information, which would allow comparison of the electron distributions with various interplanetary conditions, specifically the anisotropy noted within magnetic sectors by Pilipp and others (1985).

APPENDIX A

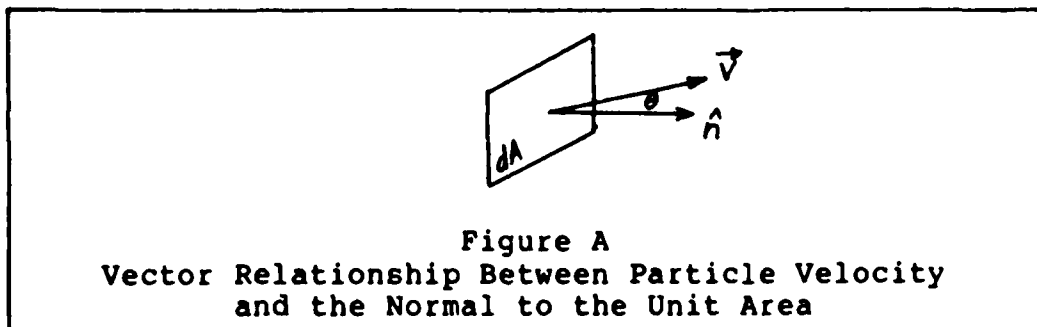
Conversion of SSJ/4 Counts to Useful Quantities

To make any useful representation of particle detector data, one must be able to convert the raw count rate to a physical parameter such as the differential flux, integral flux, or distribution function values. This Appendix outlines the justification for the standard conversion for most cylindrical electrostatic analyzers to such quantities. Much of the material herein was drawn from Denig (1982:61-64) and Marshall and others (1986:233-235).

It is known the number of particles crossing a unit area (dA) in a unit time (dt) is

$$dN = f(\vec{r}, \vec{v}, t) \vec{v} \cdot \hat{n} dA dt d^3\vec{v} \quad (\text{A-1})$$

where $f(\vec{r}, \vec{v}, t)$ represents the number of particles within a



phase space volume $d^3\vec{r}d^3\vec{v}$ at position \vec{r} with velocity \vec{v} at time t . Note $\vec{v} \cdot \hat{n}$ equals $v \cos\theta$ (see fig A). Since the look angles of the SSJ/4 are between 1° ($\cos 1^\circ = .9998$) and 5° ($\cos 5^\circ = .9962$), the small angle approximation results in

$$\vec{v} \cdot \hat{n} \approx v$$

Assuming azimuthal symmetry, which is in part justified for the SSJ/4 rectangular aperture because of the small angle approximation just cited, and in part because there are no perturbing magnetic field variations (Malcolm, 1986) over look angle during the access time of one channel, we can let $f(\vec{r}, \vec{v}, t)$ go to $f(\vec{r}, E)$ through the following:

$$\begin{aligned} E &= mv^2/2 \\ \text{so } dE &= mv \, dv \end{aligned}$$

resulting in

$$v \, d^3\vec{v} = v^2 (v \, dv) \, d\Omega = (2E/m^2) \, dE \, d\Omega \quad (\text{A-2})$$

substituting eq (A-2) into eq (A-1) and manipulating:

$$f(\vec{r}, E) = \frac{m^2 \, dN}{2E \, dE \, d\Omega \, dA \, dt} \quad (\text{A-3})$$

Defining the following quantities

- C = number of counts from detector
- g = geometric factor
- τ = sampling time of detector

and noting that $dN/dt = C/\tau$ (the count rate if the channel was sampling 100% of the time) and $g = dA \, d\Omega$, eq (A-3) takes the form

$$f(\vec{r}, E) = \frac{m^2 \, C/\tau}{2 \, E \, dE \, g}$$

Further noting the energy independent geometric factor (G) equals $g \, dE$, it is seen the value of the distribution function is proportional to count rate and inversely proportional to energy and the energy-independent geometric factor:

$$f(\vec{r}, E) = \frac{m^2 C/\tau}{2 E G} \quad (A-4)$$

Knowing the total number flux $[F(\vec{r}, t)]$ is described by the first velocity moment of the distribution function as

$$F(\vec{r}, t) = \int f(\vec{r}, \vec{v}, t) \vec{v} \cdot \hat{n} d^3\vec{v} ,$$

eq (A-2) may be substituted:

$$F(\vec{r}, t) = \int f(\vec{r}, E) 2E/m^2 dE d\Omega \quad (A-5)$$

The differential number flux $[j(r, E)]$ is defined as

$\partial^2 F / \partial E d\Omega$. Taking the partial derivatives of eq (A-5), the differential number flux is

$$j(\vec{r}, E) = f(\vec{r}, E) \frac{2E}{m^2} \quad (A-6)$$

Using the "physical" quantities from eq (A-4):

$$j(\vec{r}, E) = \frac{C/\tau}{G} \quad (A-7)$$

Since the values for the energy-independent geometric factor ($\text{cm}^2\text{-eV-sr}$) and the nominal energy are determined in calibration (Marshall and others, 1986) and tabulated for each channel (Hardy and others, 1984a:20,23), one need determine only the count rate to calculate $j(\vec{r}, E)$ and $f(\vec{r}, E)$.

Other useful quantities which rely on $j(\vec{r}, E)$ are:

(1) The integral number flux ($\text{e}^-/\text{cm}^2\text{-sr-s}$):

$$JTOT = j_1(E_1 - E_2) + \sum_{i=2}^{19} j_i \frac{E_{i-1} - E_{i+1}}{2} + j_{20}(E_{19} - E_{20}) \quad (A-8)$$

where the subscripts denote channel number and the position and energy notation has been dropped from J for convenience.

(2) The integral energy flux (keV/cm²-sr-s):

$$\text{JETOT} = E_1 j_1 (E_1 - E_2) + \sum_{i=2}^{19} E_i j_i \frac{E_{i-1} - E_{i+1}}{2} + E_{20} j_{20} (E_{19} - E_{20}) \quad (\text{A-9})$$

(3) The average energy (keV), which is simply eq (A-9) divided by eq (A-8):

$$\text{EAVE} = \frac{\text{JETOT}}{\text{JTOT}}$$

It should be noted that it is these three quantities which are displayed in fig 4 in Section IV.

At times it is useful to calculate the count rate that would result from a perfect maxwellian distribution of density n_0 and temperature T. Manipulating eq (A-4) it is seen

$$C = f(\vec{r}, E) \frac{2 E G}{m^2}$$

Plugging in the standard maxwellian form for $f(r, E)$:

$$C = \frac{2 n_0 E G \tau}{m^{1/2} (2\pi kT)^{3/2}} \exp^{-E/kT}$$

Using the appropriate constants, this may be set up in the "cookbook" form:

$$C = 5.219 \times 10^5 \frac{n_0 [\text{cm}^{-3}] E [\text{eV}] G [\text{cm}^2 - \text{eV} - \text{sr}]}{(T [\text{eV}])^{3/2}} \exp^{-E/T} \quad (\text{A-10})$$

As an example, to show how the SSJ/4 sensor should

TABLE A

Count Rate Generated by a Perfect Double
Maxwellian Distribution

CHANNEL	ENERGY(eV)	Count Rate		TOTAL
		from T_1	from T_2	
1	30180 eV	0 *	.0133	.0133
2	20620	0 *	.0711	.0711
3	14040	0 *	.187	.187
4	9580	0 *	.290	.290
5	6500	0 *	.330	.330
6	4420	0 *	.282	.282
7	3050	0 *	.205	.205
8	2060	0 *	.141	.141
9	1410	0 *	.0822	.0822
10	984	.0042	.0506	.0548
11	992	.0012	.0154	.0166
12	679	.0312	.00889	.0401
13	462	.249	.00495	.254
14	317	.718	.0024	.718
15	213	1.16	.0011	1.16
16	145	1.18	.0005	1.18
17	100	.851	.0002	.851
18	68	.505	0 *	.505
19	46	.234	0 *	.234
20	32	.106	0 *	.106

* count rates less than 10^{-4}

respond to a perfect double maxwellian, the predicted count rates are generated in Table A for $T_1=80$ eV, $n_1=0.017$ cm⁻³, $T_2=4300$ eV and $n_2=0.00046$ cm⁻³. These numbers are the results from a March 16, 1983 satellite pass, but should not be interpreted as typical values (see Section V: Results).

The key result to be seen in this Table is that for a bi-maxwellian distribution, the count rate increases and then falls off in each analyzer, with the peak occurring in the channel with slightly less energy than double the temperature of the maxwellian. Also note the count rate in the

992 eV (chan 11) and the 30 keV (chan 1) channels is extremely small, about one count per 60 seconds of data accumulation. Further, for most double maxwellian distributions, counts in channels 1-9 may be thought of as belonging strictly to the high energy component, while counts in channels 16-20 are attributed to the low energy component. Channels 9-15 (213 eV - 1.41 keV) become transition channels.

APPENDIX B

Noise Correction

The noise correction to the DMSP-F6 data set is outlined via the following algorithm format. A lettered step involved test runs or literature research and resulted in a decision or assumption. A numbered step was actually coded into the analysis software.

Step A: Perform least-squares fits on distribution function values with no background correction, and determine the temperature for channels 1-10. For approximately 40 test runs the temperature was commonly 4-6 keV, with the temperature exceeding 7.5 keV twice. Since noise in the two highest energy channels will seem to make the distribution hotter than it really is, assume the high energy component never has a temperature above 7.5 keV.

Step B: Calculate the relative count rate that would be generated by a perfect maxwellian of 7.5 keV (the absolute count rate is density dependent). Note the count rate in channel 1 would be less than any channel 2 through 7 and the count rate in channel 2 would be less than any channel 3 through 5. Also note the count rate for channels 1 and 2 averaged would be less than channels 4-9 averaged. Finally, note the ratio between channel 2 and 1 would be 2.07 : 1.

Step 1: Determine if channels 1 and 2 are noisy by comparing their averaged count rate to the average for channels 4 through 9. If the channel 1 and 2 average is higher, an instrumental noise correction must be made. If the average is lower skip to Step 6.

Step 2: Determine the lowest count rate in channels 2 through 7. Correct channel 1 to this count rate plus its Poisson error (square root of the count rate), because this is the controlling statistic in any detector in the low count regime.

Step 3: If the ratio of channel 2 to the corrected channel 1 is greater than 2.07, channel 2 is also noisy and it is corrected to 2.07 times the corrected channel 1

count rate.

- Step 4: Determine the lowest count rate in channels 3 through 5. If the present channel 2 count rate is greater than the lowest count rate plus its Poisson error, then correct channel 2 to this value.
- Step 5: If a correction was made in Step 4, see if channel 1 is less than 0.483 times channel 2. If not, correct channel 1 to this value.

Perform iterative technique on the natural background as outlined in Section IV: Data Analysis.

- Step 6: Assume the natural background is zero.
- Step 7: Subtract the background from channels 1-10.
- Step 8: Fit channels 1-10 to a maxwellian distribution. Determine the temperature and density from the fit, and use them to predict the count rate for channel 1 (see eq [A-10]).
- Step 9: Use the "real" count rate for channel 1 to determine the predicted natural background (total count rate - "real" count rate = background). Compare this with the assumed background, and if their difference is not within a 1 count (per time interval) tolerance, make the predicted background the new assumption and go to Step 7.
- Step 10: Subtract 1/10 (the ratio of the cross-sectional area of the channeltrons of the low and high energy analyzers [Gussenhoven and others, 1984:9788]) of the background from the low energy analyzer.
- Step C: It was noted in test runs that channels 11 and 12 were noisy. Channels 10 and 13 were noted to be relatively clean. Since their nominal energies are nearly the same, it may be shown (using eq [A-10]) that for any electron distribution the count rate in channel 10 should be 3.3 times the channel 11 count rate (simply the ratio of their energy-independent geometric factors). From Riehl and Hardy (1986) it is known the low energy component has a mean temperature of 82 eV. Assuming this temperature, eq (A-10) may be used to show the ratio of channel 13 to channel 12 should be about 7.
- Step D: Test runs on channels 10-13 indicated noise levels fluctuated on a month-to-month basis. It was decided to perform the noise corrections on a half-

month basis.

Step 11: Plot the ratios of adjacent channels (10/11, 12/13) versus the clean channel (10,13) as in fig B.

Step E: Determine the corrections to channels 11 and 12 in the following manner (after Hardy and others, 1984a), using the results in fig B as an example:

Using a linear regression, fig B1 shows the best fit was

$$\frac{CR_{10M}}{CR_{11M}} = 1.409 CR_{10M} - 0.0167 \quad (B-1)$$

where CR refers to the count rate of the noted channel, and the subscript M = 'measured', meaning the noise contaminated measurement. From Step C, it is known

$$CR_{10T} = 3.3 CR_{11T} \quad (B-2)$$

where the subscript T = 'theoretical', meaning a noise free measurement. Channel 10 has been noted to be noise free, so

$$CR_{10M} = CR_{10T} \quad (B-3)$$

Substituting eq (B-3) into eq (B-2), and then into eq (B-1):

$$\frac{3.3 CR_{11T}}{CR_{11M}} = 1.409 (3.3 CR_{11T}) - .0167$$

Manipulating this, it can be shown

$$CR_{11T} = .00506 \frac{CR_{11M}}{1.409 CR_{11M} - 1} \quad (B-4)$$

In this way, the noise contaminated data may be corrected in a systematic fashion.

Usually the relationship between the ratio and the clean channel could not be explained by a simple linear-linear representation. As shown in figure B2, the \log_{10} - \log_{10} representation produced the best linear fit. This type of relationship was corrected for noise as follows (where 'log' represents \log_{10}):

MAY, 1983

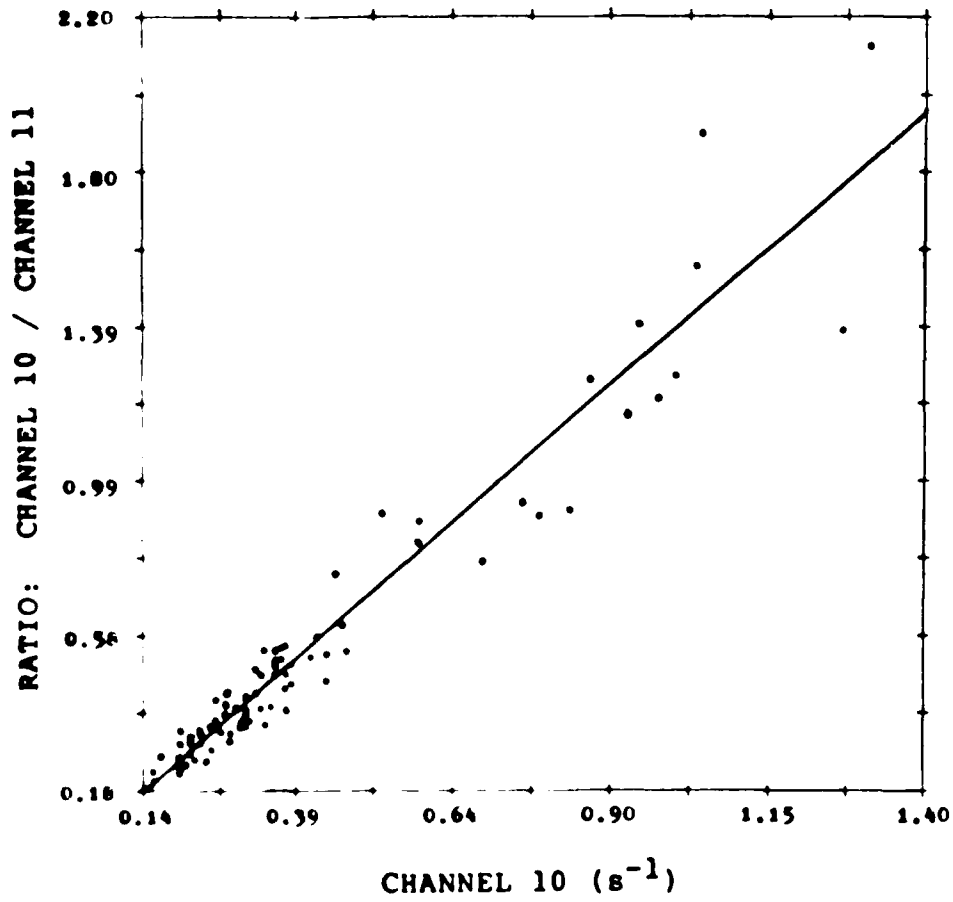


Figure B-1
Noise Analysis
Channel 11

MAY, 1983

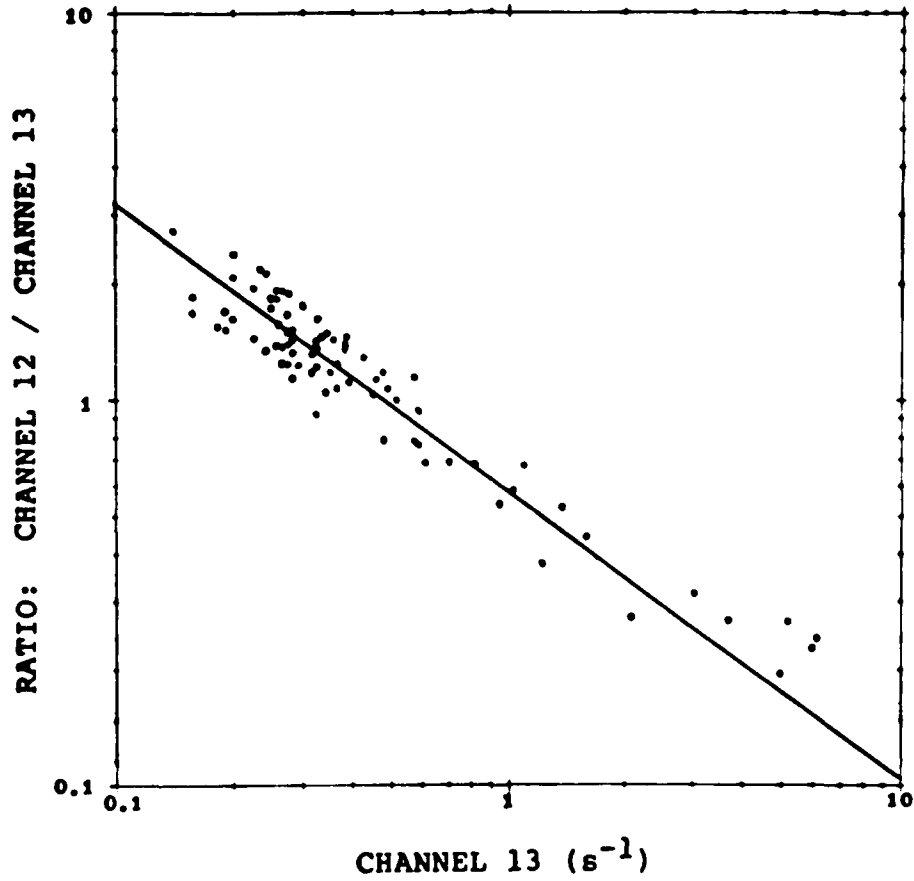


Figure B-2
Noise Analysis
Channel 12

$$\log \left(\frac{CR12_M}{CR13_M} \right) = -0.729 \log CR13_M - 0.233$$

or

$$\log CR12_M = 0.271 \log CR13_M - 0.233 \quad (B-5)$$

From Step C it is known

$$CR13_T \approx 7 CR12_T \quad \text{and} \quad CR13_T = CR13_M$$

Substituting these into eq (B-5), it can be shown that

$$CR12_T = 10^{(3.69 \log CR12_M + 0.0147)} \quad (B-6)$$

Step 12: Correct channels 11 and 12 for instrumental noise. A summary of the corrections for each half-month (in the form of eq [B-4] or eq [B-6]) is shown in Table B.

Step 13: Correct the three lowest energy channels (18-20) per Hardy and others (1984a:48).

This completes the noise corrections used in this study.

TABLE B

Summary of Systematic Corrections for
Noise in Channels 11 and 12

January 1-15, 1983:

Chan 11: no correction possible

Chan 12: $CR_{12T} = 10^{(3.416 \log CR_{12M} - 0.966)}$

February 1-14, 1983:

Chan 11: no correction possible

Chan 12: $CR_{12T} = 10^{(2.186 CR_{12M} - 0.863)}$ *

March 16-31, 1983:

Chan 11: $CR_{11T} = \frac{CR_{11M}}{1.409 CR_{11M} - 1}$

Chan 12: $CR_{12T} = 10^{(3.69 \log CR_{12M} + 0.0147)}$

May 16-31, 1983:

Chan 11: $CR_{11T} = 10^{(-10.953 \log CR_{11M} - 4.002)}$

Chan 12: $CR_{12T} = 10^{(8.036 \log CR_{12M} + 3.385)}$ **

* used only for $CR_M < 1.85$

** used only for $CR_M < 2.0$

BIBLIOGRAPHY

- Allen, Joe H. "Major Magnetic Storm Effects Noted," EOS, 67: 573 (June, 1986).
- Akasofu, S.-I. and L.-C. Lee. A Study of the Relationship Between Solar Activity and Interplanetary Field Variations, Technical Report AFGL-TR-86-0032. Air Force Geophysics Laboratory (AFSC), Hanscom AFB, MA, February, 1986.
- Akasofu, S.-I. and C.F. Fry. Development of a Geomagnetic Storm Prediction Scheme-Phase I, Technical Report AFGL-TR-85-0152. Air Force Geophysics Laboratory (AFSC), Hanscom AFB, MA, June, 1985.
- Akasofu, S.-I. "Solar-Wind Disturbances and the Solar Wind Magnetosphere Energy Coupling Function," Space Science Reviews, 34: 173-183 (February, 1983).
- Akasofu, S.-I. and D.N. Covey, C.-I. Meng. "Dependence of the Geometry of the Region of Open Field Lines on the Interplanetary Magnetic Field," Planetary and Space Science, 29: 803-807 (August, 1981).
- Akasofu, Syun-Ichi. Polar and Magnetospheric Substorms. Springer-Verlag, New York, 1968.
- Axford, W.I. "The Solar Wind," Solar Physics, 100: 575-586 (October, 1985).
- Axford, W.I. "Magnetic Field Reconnection," Magnetic Reconnection in Space and Laboratory Plasmas, edited by Edward W. Hones, Jr. 1-8. Geophysical Monograph 30, American Geophysical Union, Washington D.C., 1984.
- Baker, D.N. and S.J. Bame, W.C. Feldman, J.T. Gosling, R.D. Zwickl, J.A. Slavin, E.J. Smith. "Strong Electron Bidirectional Anisotropies in the Distant Tail: ISEE 3 Observations of the Polar Rain," Journal of Geophysical Research, 91: 5637-5662 (May, 1986).
- Baker, D.N. and E.W. Hones, Jr., J.B. Payne, W.C. Feldman. "A High Time Resolution Study of Interplanetary Parameter Correlations With AE," Geophysical Research Letters, 8: 179-182 (February, 1981).
- Bame, S.J. and R.C. Anderson, J.R. Asbridge, D.N. Baker, W.C. Feldman, J.T. Gosling, E.W. Hones, Jr., D.J. McComas, R.D. Zwickl. "Plasma Regimes in the Deep Geomagnetic Tail: ISEE 3," Geophysical Research Letters, 10: 912-915 (September, 1983).

- Barfield, J.N. Magnetospheric Plasma Studies Using Data from the Dynamics High and Low Altitude Plasma Instruments, Technical Report AFGL-TR-84-0136. Air Force Geophysics Laboratory (AFSC), Hanscom AFB, MA, May, 1984.
- Bevington, Philip R. Data Reduction and Error Analysis for the Physical Sciences. McGraw-Hill, New York, 1969.
- Burke, William J. and David A. Hardy, Roger P. Vancour. Magnetospheric and High-Latitude Ionospheric Electrodynamics, Technical Report AFGL-TR-82-0131. Air Force Geophysics Laboratory (AFSC), Hanscom AFB, MA, April, 1982.
- Cattell, C.A. and F.S. Mozer, E.W. Hones, Jr., R.R. Anderson, R.D. Sharp. "ISEE Observations of the Plasma Sheet Boundary, Plasma Sheet, and Neutral Sheet 1. Electric Field, Magnetic Field, Plasma and Ion Composition," Journal of Geophysical Research, 91: 5663-5680 (May, 1986).
- Couzens, David A. and Joseph H. King. Interplanetary Medium Data Book-Supplement 3A, 1977-1985. National Space Science Data Center (NSSDC), NASA Goddard Space Flight Center, MD, April, 1986.
- Cowley, S.W.H. "Asymmetry Effects Associated With the X-Component of the IMF in a Magnetically Open Magnetosphere," Planetary and Space Science, 29: 809-818 (August, 1981a).
- Cowley, S.W.H. "Magnetospheric Asymmetries Associated with the Y-Component of the IMF," Planetary and Space Science, 29: 79-96 (January, 1981b).
- Cowley, S.W.H. "A Qualitative Study of the Reconnection Between the Earth's Magnetic Field and an Interplanetary Field of Arbitrary Orientation," Radio Science, 8: 903-913 (November, 1973).
- Cuperman, S. "Solar Wind Theory," Space Science Reviews, 34: 63-72 (January, 1983).
- Denig, William F. Waves and Particle Observations Associated with Beam Plasma Discharge in a Space Simulation Chamber. PhD Dissertation. Utah State University, Logan, UT, October, 1982.
- Dungey, J.W. "Interplanetary Field and the Auroral Zones," Physical Review Letters, 6: 47-52 (January 15, 1961).

- Eastman, T.E. and E.W. Hones, Jr., S.J. Bame, J.R. Asbridge. "The Magnetospheric Boundary Layer: Site of Plasma, Momentum and Energy Transfer from the Magnetosheath into the Magnetosphere," Geophysical Research Letters, 3: 685-689 (November, 1976).
- Fairfield, D.H. and J.D. Scudder. "Polar Rain: Solar Coronal Electrons in the Earth's Magnetosphere," Journal of Geophysical Research, 90: 4055-4068 (May, 1985).
- Feldman, W.C. and J.R. Asbridge, S.J. Bame, J.T. Gosling, R.D. Zwickl. "Electron Heating at Interplanetary Shocks," Solar Wind Five, edited by M. Neugebauer. 403-411. NASA Conference Publication 2280, Washington D.C., 1983.
- Feldman, W.C. and J.R. Asbridge, S.J. Bame, J.T. Gosling, D.S. Lemons. "Characteristic Electron Variations Across Simple High-Speed Solar Wind Streams," Journal of Geophysical Research, 83: 5285-5295 (November, 1978).
- Feldman, W.C. and J.R. Asbridge, S.J. Bame, M.D. Montgomery, S.P. Gary. "Solar Wind Electrons," Journal of Geophysical Research, 80: 4181-4196 (October, 1975).
- Fremouw, E.J. and L.A. Wittwer. "The HILAT Satellite Program: Introduction and Objectives," Johns Hopkins APL Technical Digest, 5: 98-103 (April, 1984).
- Gosling, J.T. and D.N. Baker, S.J. Bame, R.D. Zwickl. "Bidirectional Solar Wind Electron Heat Flux and Hemispherically Symmetric Polar Rain," Journal of Geophysical Research, XX: XXXX-XXXX (October, 1986).
- Gussenhoven, M.S. and D.A. Hardy, N. Heinemann, R.K. Burkhardt. "Morphology of the Polar Rain," Journal of Geophysical Research, 89: 9785-9800 (November, 1984).
- Hardy, D.A. and M.S. Gussenhoven, E. Holeman. "A Statistical Model of Auroral Electron Precipitation," Journal of Geophysical Research, 90: 4229-4248 (May, 1985).
- Hardy, D.A. and L.K. Schmitt, M.S. Gussenhoven, F.J. Marshall, H.-C. Yeh, T.L. Schumaker, A. Huber, J. Pantazis. Precipitating Electron and Ion Detectors (SSJ/4) for the Block 5D/Flights 6-10 DMSP Satellites: Calibration and Data Presentation, Technical Report AFGL-TR-84-0317. Air Force Geophysics Laboratory (AFSC), Hanscom AFB, MA, November, 1984a.

- Hardy, David A. "Intense Fluxes of Low-Energy Electrons at Geomagnetic Latitudes Above 85°," Journal of Geophysical Research, 89: 3883-3899 (April, 1984b).
- Hardy, David A. and Alan Huber, John A. Pantzias. "The Electron Flux J Sensor for HILAT," Johns Hopkins APL Technical Digest, 5: 125-130 (April, 1984c).
- Heikkila, Walter J. "Magnetospheric Topology of Fields and Currents," Magnetospheric Currents, edited by T. Potemra. 208-227. Geophysical Monograph 28, American Geophysical Union, Washington D.C., 1984.
- Heikkila, Walter J. and J. David Winningham. Auroral Data Analysis, Technical Report AFCL-TR-74-0379. Air Force Cambridge Research Laboratories (AFSC), Hanscom AFB, MA, September, 1974.
- Heinemann, N. and M.S. Gussenhoven, D.A. Hardy, R.H. Redus, H.-C. Yeh. "Auroral Particle Precipitation During a 24 Hour Change From Strong IMF B_z Southward to Strong IMF B_z Northward", Presented at the Spring American Geophysical Union Meeting, Baltimore, MD, May, 1986.
- Hudson, P.D. "The Reflection of Charged Particles by Rotational Discontinuities," Planetary and Space Science, 22: 1571-1577 (November, 1974).
- Hudson, P.D. "Rotational Discontinuities in an Anisotropic Plasma--II," Planetary and Space Science, 21: 475-483 (March, 1973).
- Malcolm, Perry, Project Scientist, Space Physics Division. Telephone interviews. Air Force Geophysics Laboratory (AFSC), Hanscom AFB, MA, September, 1986.
- Marshall, F.J. and D.A. Hardy, A. Huber, J. Pantzias, J. McGarity, E. Holeman, J.D. Winningham. "Calibration System for Electron Detectors in the Energy Range From 10 eV to 50 keV," Reviews of Scientific Instruments, 57: 229-235 (February, 1986).
- Meng, Ching-I. "The Auroral Electron Precipitation During Extremely Quiet Geomagnetic Conditions," Journal of Geophysical Research, 86: 4607-4627 (June, 1981).
- Meng, C.-I. and S.-I. Akasofu, K.A. Anderson. "Dawn-Dusk Gradient of the Precipitation of Low-Energy Electrons Over the Polar Cap and its Relationship to the Interplanetary Magnetic Field," Journal of Geophysical Research, 82: 5277-5293 (November, 1977).

- Nishida, A. "IMF Control of the Earth's Magnetosphere," Space Science Reviews, 14: 185-200 (February, 1983).
- Ober, William E. Statistical Analysis of Low Energy Electrons and Their Relationship to Radiowave Scintillations. MS Thesis, School of Engineering, Air Force Institute of Technology (AU), Wright-Patterson AFB, OH, December, 1984.
- O'Brien, B.J. "Comments on Measurements of Particle Precipitation with the INJUN Satellites," High Latitude Particles and the Ionosphere, edited by B. Maehlum. 113-118. Academic Press, New York, 1965.
- Parker, E.N. "Kinetic Properties of Interplanetary Matter," Planetary and Space Science, 9: 461-475 (August, 1962).
- Phillips, Charles D. Systematics of the Auroral Boundary as Indicated by Particle Precipitation. MS Thesis, School of Engineering, Air Force Institute of Technology (AU), Wright-Patterson AFB, OH, December, 1984.
- Pilipp, W.G. and H. Miggenrieder, K.-H. Muhlhauser, H. Rosenbauer, R. Schwenn, F.M. Neubauer. "Variations of Electron Distribution Functions in the Solar Wind," submitted to the Journal of Geophysical Research (1985).
- Pneuman, G.W. "Driving Mechanisms for the Solar Wind," Space Science Reviews, 43: 105-138 (February, 1986).
- Riehl, Kevin B. and David A. Hardy. "Average Characteristics of the Polar Rain and Their Relationship to the Solar Wind and the Interplanetary Magnetic Field," Journal of Geophysical Research, 91: 1557-1571 (February, 1986).
- Rosenbauer, H. and R. Schwenn, E. Marsch, B. Meyer, HH. Miggenrieder, M.D. Montgomery, K.H. Muhlhauser, W. Pilipp, W. Voger, S.M.Zink. "A Survey on Initial Results of the HELIOS Plasma Experiment," Journal of Geophysical Research, 42: 561-580 (1977).
- Schmidt, George. Physics of High Temperature Plasmas. Academic Press, New York, 1979.
- Schulz, M. and L.J. Lanzerotti. Particle Diffusion in the Radiation Belts. Springer-Verlag, New York, 1974.
- Scudder, Jack D. and Stanislaw Olbert. "A Theory of Local and Global Processes Which Affect Solar Wind Electrons 2. Experimental Support," Journal of Geophysical Research, 84: 6603-6620 (November, 1979).

- Slavin, J.A. and B.T. Tsurutani, E.J. Smith, D.E. Jones, D.G. Sibeck. "Average Configuration of the Distant (<220 R_e) Magnetotail: Initial ISEE-3 Magnetic Field Results," Geophysical Research Letters, 10: 973-976 (October, 1983).
- Stern, David P. "Magnetospheric Dynamo Processes," Magnetospheric Currents, edited by T. Potemra. 200-207. Geophysical Monograph 28, American Geophysical Union, Washington D.C., 1984.
- Van Allen, J.A. and G.H. Ludwig, E.C. Ray, C.E. McIlwain. "Observation of High Intensity Radiation by Satellites 1958 Alpha and Gamma," Jet Propulsion, 28: 588-592 (September, 1958).
- Winningham, J.D. and W.J. Heikkila. "Polar Cap Auroral Electron Fluxes Observed with ISIS 1," Journal of Geophysical Research, 79: 949-965 (February, 1974).
- Yeager, D.M. and L.A. Frank. "Low Energy Electron Intensities at Large Distances Over the Earth's Polar Caps," Journal of Geophysical Research, 81: 3966-3978 (June, 1976).

VITA

Kevin Bruce Riehl was born in Detroit, Michigan on July 7, 1958. He grew up in Westland, Michigan and graduated from Livonia Franklin High School in 1976. He attended the Massachusetts Institute of Technology and attained a Bachelor of Science in Physics and a commission in the United States Air Force in June, 1980. His assignment prior to the Air Force Institute of Technology was in the Space Physics Division, Air Force Geophysics Laboratory, Hanscom AFB, MA.

Captain Riehl is a member of the American Geophysical Union, Sigma Xi, and Tau Beta Pi. He is married to the former Dianne L. Segien and has one child, Brian. His next assignment is to the Air Force Technical Applications Center, Patrick AFB, FL.

Permanent address: 8307 Donna

Westland, Michigan 48185

REPORT DOCUMENTATION PAGE

Form Approved
OMB No 0704-0188

1a. REPORT SECURITY CLASSIFICATION Unclassified		1b. RESTRICTIVE MARKINGS	
2a. SECURITY CLASSIFICATION AUTHORITY		3. DISTRIBUTION / AVAILABILITY OF REPORT Approved for public release; distribution unlimited	
2b. DECLASSIFICATION / DOWNGRADING SCHEDULE		5. MONITORING ORGANIZATION REPORT NUMBER(S)	
4. PERFORMING ORGANIZATION REPORT NUMBER(S) AFIT/GEP/ENP/86D-8		7a. NAME OF MONITORING ORGANIZATION	
6a. NAME OF PERFORMING ORGANIZATION School of Engineering	6b. OFFICE SYMBOL (If applicable) AFIT/ENP	7b. ADDRESS (City, State, and ZIP Code) Approved for public release LAW AFB 100-11 E. WOLAVER Dean for Research and Professional Development	
8a. NAME OF FUNDING / SPONSORING ORGANIZATION Space Physics Division	8b. OFFICE SYMBOL (If applicable) AFGL/PHP	9. PROCUREMENT INFORMATION AND IDENTIFICATION NUMBER	
8c. ADDRESS (City, State, and ZIP Code) Air Force Geophysics Laboratory Hanscom AFB, MA 01731		10. SOURCE OF FUNDING NUMBERS	
		PROGRAM ELEMENT NO 62101F	PROJECT NO 7601
		TASK NO 12	WORK UNIT ACCESSION NO 03
11. TITLE (Include Security Classification) INVESTIGATIONS OF THE POLAR RAIN: POLAR CAP ELECTRON PRECIPITATION			
12. PERSONAL AUTHOR(S) Kevin B. Riehl, B.S., Capt, USAF			
13a. TYPE OF REPORT MS Thesis	13b. TIME COVERED FROM _____ TO _____	14. DATE OF REPORT (Year, Month, Day) 1986 December	15. PAGE COUNT 93
16. SUPPLEMENTARY NOTATION			
17. COSATI CODES		18. SUBJECT TERMS (Continue on reverse if necessary and identify by block number)	
FIELD 20	GROUP 09	Electron precipitation; Solar wind; Interplanetary magnetic fields; Polar caps	
19. ABSTRACT (Continue on reverse if necessary and identify by block number) A study of the characteristics of the polar rain using data from the SSJ/4 sensor on the Defense Meteorological Satellite Program F6 satellite has been performed. Recent literature on the polar rain is reviewed. Dawn/Dusk flux gradients are verified as being controlled by the interplanetary magnetic field (IMF) Y-component at least 84% of the time. The IMF Z-component is shown to play a role in generating flux gradients. The polar rain is best characterized by a double maxwellian distribution with typical temperatures of 80-90 eV for the low energy component and 3.6-4.8 keV for the high energy component. The characteristics of the low energy component of the polar rain strongly match those of the solar wind strahl component, suggesting the polar rain is of strahl origin. But correlations with IMF sector structure and solar wind parameters do (continued on reverse side)			
20. DISTRIBUTION / AVAILABILITY OF ABSTRACT <input checked="" type="checkbox"/> UNCLASSIFIED/UNLIMITED <input type="checkbox"/> SAME AS RPT <input type="checkbox"/> DTIC USERS		21. ABSTRACT SECURITY CLASSIFICATION Unclassified	
22a. NAME OF RESPONSIBLE INDIVIDUAL James A. Lupo, Major, USAF		22b. TELEPHONE (Include Area Code) 513-255-4498	22c. OFFICE SYMBOL AFIT/ENP

not show the relationships proposed by Fairfield and Scudder (Journal of Geophysical Research, 1985), since the "unpreferred" cap generally has the same polar rain characteristics as the "preferred" cap.

END

4-87

DTIC